On the Cool Side: Modeling the Atmospheres of Brown Dwarfs and Giant Planets

M.S. Marley and T.D. Robinson

NASA Ames Research Center, Moffett Field, California 94035;
email: Mark.S.Marley@nasa.gov, Tyler.D.Robinson@nasa.gov

Keywords

extrasolar planets, radiative transfer, convection, chemistry, clouds, opacity

Abstract

The atmosphere of a brown dwarf or extrasolar giant planet controls the spectrum of radiation emitted by the object and regulates its cooling over time. Although the study of these atmospheres has been informed by decades of experience modeling stellar and planetary atmospheres, the distinctive characteristics of these objects present unique challenges to forward modeling. In particular, complex chemistry arising from molecule-rich atmospheres, molecular opacity line lists (sometimes running to 10 billion absorption lines or more), multiple cloud-forming condensates, and disequilibrium chemical processes all combine to create a challenging task for any modeling effort. This review describes the process of incorporating these complexities into one-dimensional radiative-convective equilibrium models of substellar objects. We discuss the underlying mathematics as well as the techniques used to model the physics, chemistry, radiative transfer, and other processes relevant to understanding these atmospheres. The review focuses on methods for creating atmosphere models and briefly presents some comparisons of model predictions to data. Current challenges in the field and some comments on the future conclude the review.

1. INTRODUCTION

The atmosphere of a brown dwarf or giant planet, despite constituting a negligible fraction of the total mass, plays a crucial role in controlling the evolution and appearance of the object. By connecting the deep, convective interior with the thermal radiation pouring out from the object, the atmosphere regulates how quickly the interior can cool over time. The atmosphere also imprints the varied signatures of gases, condensates, gravity, and the temperature profile onto emitted thermal radiation, thereby controlling the spectral signature of the object. Thus, understanding the spectrum and evolution over time of a giant planet or brown dwarf requires a working knowledge of the atmosphere. Especially for freely floating brown dwarfs, almost everything we know about an object depends upon our ability to understand its atmosphere.

However, the atmospheres of brown dwarfs and giant planets are complex. Because these bodies are relatively cool (by stellar standards), chemical equilibrium favors the formation of molecules that often have opacities that vary strongly with wavelength. In addition, at these temperatures condensates can form, adding the seemingly intractable complexity of cloud physics to the problem. Unlike stellar atmospheres, where "photospheres" (or the region over which thermal optical depth is near unity) are typically well defined, the strongly wavelength-dependent opacity in brown dwarf and giant planet atmospheres leads to photospheres that vary with wavelength, and physical locations that can vary by several pressure scale heights.

The aim of this review is to discuss the techniques, and challenges, related to the construction of model atmospheres for brown dwarfs and young giant planets. For specificity, we consider those processes that influence the atmospheres of the L, T, and Y dwarf spectral types as well as the directly imaged planets. We explore influences on the thermal structure, composition, and energy transport in these objects. Although our focus is primarily on self-luminous objects, we also briefly consider the problem of absorption of incident light, which is relevant to worlds orbiting a primary star.

In this review we consider the problem of constructing a self-consistent, one-dimensional atmospheric structure model that converts a given internal heat flux from the deep, convective interior to radiation that departs the top of the atmosphere. This type of model is usually termed a radiative-convective model, and it aims to represent, as an average, the complex three-dimensional structure of the atmosphere. We explore how gravity, atmospheric composition, gaseous and cloud opacity, and incident flux all influence the thermal profile and spectra of emitted radiation. We demonstrate the utility such models have for the interpretation of observations and also consider their limitations for studying complex problems, including time variability and atmospheric dynamics.

A number of previous reviews have covered topics related to radiative-convective modeling of planetary and substellar atmospheres. Of historical interest are reviews by Pecker (1965), who discusses modeling of stellar atmospheres, and Vardya (1970), who examines properties and modeling of low-mass stars. Several decades after these reviews, Allard et al. (1997) revisited models and spectroscopic properties of very low-mass stars. These authors also discussed early work in the modeling of brown dwarfs, including grain formation and opacity. Of course, techniques and data for the modeling of condensates, gas and grain opacities, and radiative transfer have progressed substantially in the intervening years.

As the atmosphere controls the cooling rate of the interior, an understanding of brown dwarf or giant exoplanet evolution crucially depends upon the construction of realistic, nongray atmosphere models for describing the surface boundary condition (Saumon et al. 1994, Chabrier & Baraffe 1997). The evolution of very low-mass stars and brown dwarfs is reviewed by Burrows et al. (2001), whereas Saumon & Marley (2008) present more recent calculations. Burrows et al.

(2001) review the data and techniques for computing atmospheric chemistry, abundances, and opacities; compare several cloud models; and review exoplanet and brown dwarf evolution and spectral properties. Kirkpatrick (2005) more completely discusses L and T dwarf colors and spectra and the classification of such objects.

The theory of giant planets, emphasizing interior structure, evolution, and what we have learned from studying Jupiter and Saturn, is explored by Hubbard et al. (2002). Very recently, Helling & Casewell (2014) reviewed the current state of brown dwarf observations, and they discuss related modeling with an emphasis on clouds, including a comparison of a number of cloud models. Finally, Catling (2015) reviews the physics of planetary atmospheres, with an emphasis on Solar System worlds, and the equations and processes that govern atmospheric composition, chemistry, thermal structure, radiative transfer, and circulation.

One reason that the study of cool atmospheres is especially interesting is that it lies at the frontier of two fields: astronomy and planetary science. Indeed, among the early theoretical examinations of the first indisputable brown dwarf, Gliese 229B, one set of models (Marley et al. 1996) had a heritage traceable to studies of the atmospheres of Titan and Earth, whereas two others (Allard et al. 1996, Tsuji et al. 1996) relied on modified stellar atmosphere codes. This convergence of theory from both hot stellar atmospheres and cold planetary atmospheres toward what had once been a no man's land of atmospheric structure theory (in the realm of effective temperatures of around 500–2,500 K) has enhanced the field and provided valuable checks and balances to the theoretical development. This review aims to provide a guide for exploration of this new and interesting territory.

We begin this review with an overview of the physics that govern radiative-convective modeling of brown dwarfs and giant planets (Section 2). Following this, we discuss, in turn, the processes that are central to constructing a proper one-dimensional physical model: radiative transfer (Section 3), convection (Section 4), atmospheric chemistry (Section 5), gas opacities (Section 6), and cloud formation and condensate opacities (Section 7). Of course, each of these topics could easily merit their own dedicated review, and the references to classic papers and textbooks cited in this review provide excellent opportunities for more detailed follow-up reading. We then outline how these physics are used to actually derive a thermal profile and present some relevant data-model comparisons. Finally, we conclude with a discussion of some current issues and prospects for the future.

2. PHYSICS OVERVIEW

Our focus specifically on atmospheres of brown dwarfs and giant planets simplifies our discussion to the physics of predominantly hydrogen-helium objects, which have been relatively well studied. This review takes the perspective that the atmosphere is a semi-infinite column of gas in hydrostatic equilibrium. The goal is to understand how the gravity, internal heat, energy transport mechanisms, composition, and cloud structures of such an atmosphere influence the thermal profile and, consequently, the properties of its emitted radiation.

Figure 1 shows a schematic of a one-dimensional model atmosphere. The vertical coordinate is pressure, P, which is defined on a grid of model levels. When the gravitational force acting on any given atmospheric slab is balanced by the vertical pressure gradient force, the fluid atmosphere is in hydrostatic equilibrium and obeys

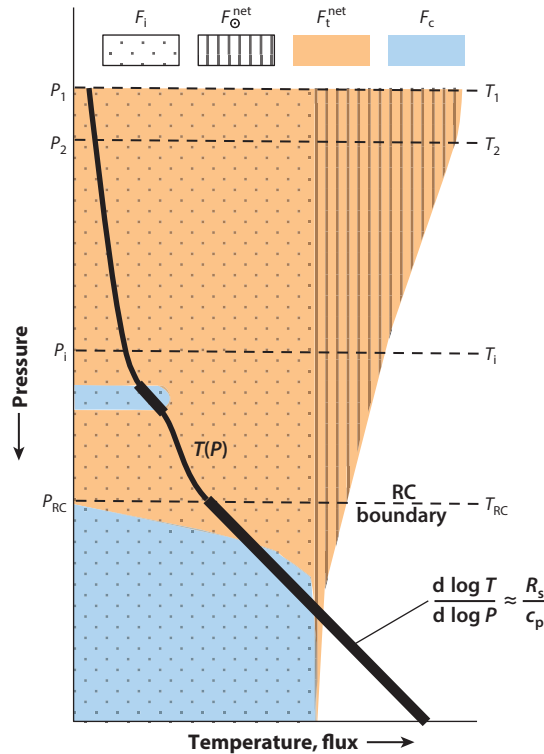$$\frac{\mathrm{d}P}{\mathrm{d}z} = -g\rho, \qquad (1)$$

Figure 1

Schematic depiction of a thermal structure model. The vertical axis is pressure, increasing downward, which is the independent variable, and the horizontal axis shows, relatively, temperature and energy flux. Model levels are shown (*horizontal dashed lines*), and the solid line is the thermal structure (i.e., temperature) profile, in which bolded lengths indicate a convective region. Level pressures and temperatures are indicated with associated subscripted symbols, and "RC" indicates the radiative-convective boundary. In equilibrium, net thermal flux (F_t^{net}, *orange*) and the convective flux (F_c, *blue*) must sum to the internal heat flux (F_i, *dotted*) and, for an irradiated object, the net absorbed stellar flux ($F_\odot^{net}$, *striped*). Note that the internal heat flux is constant throughout the atmosphere, whereas the schematic profile of net absorbed stellar flux decreases with increasing pressure; it eventually reaches zero in the deep atmosphere. At depth, convection carries the vast majority of the summed internal and stellar fluxes but is a smaller component in detached convective regions (*upper blue region*).

where z is altitude, g is the acceleration due to gravity, and ρ is the atmospheric mass density. After inserting the ideal gas law and rearranging, this expression becomes

$$\frac{dP}{P} = -\frac{gm}{k_B T}dz = -\frac{dz}{H}, \tag{2}$$

where m is the mean molecular mass in the atmosphere, k_B is Boltzmann's constant ($k_B = 1.381 \times 10^{-16}$ erg K^{-1}), and T is temperature. Here we have also defined the atmospheric pressure scale height, $H = k_B T/mg$, which, for an isothermal layer of the atmosphere, is the e-folding distance for pressure, such that the pressure-altitude relation is

$$P(z) = P(z_0)e^{-(z-z_0)/H}, \tag{3}$$

COLUMN DENSITIES

A useful quantity derived using the equation of hydrostatic equilibrium (Equation 1) is the column mass, which is the integrated mass per unit area above a given atmospheric level, given by $\mathcal{M} = \int_z^\infty \rho \, dz = P(z)/g$. The column molecular number density, $\mathcal{N}$, can be similarly defined and, using the integral definition, the equation of hydrostatic equilibrium and assuming an isothermal atmosphere, the column number density is related to the number density profile simply by $\mathcal{N} = n(z)H$. This quantity is especially helpful when estimating optical depths—given an absorption cross section per molecule, σ_a, the optical depth is roughly $\tau(z) = \sigma_a \mathcal{N}(z)$.

where $P(z_0)$ and z_0 are the pressure and altitude at the base of the layer, respectively. Thus, the physical distance between two adjacent model pressure levels shown in **Figure 1** can be determined using the layer pressure scale height and Equation 3 (see the sidebar, Column Densities).

Pressure- or altitude-dependent atmospheric properties, such as temperature (shown in **Figure 1**), chemical composition, or wavelength-dependent thermal flux, are determined either at the model levels or for the model layers (i.e., at the level midpoints). A key model input parameter is the internal heat flux, F_i, which, for a nonirradiated world, sets the effective temperature via $\sigma T_{\text{eff}}^4 = F_i$, where σ is the Stefan-Boltzmann constant (5.67×10^{-5} erg cm^{-2} s^{-1} K^{-4}). In steady state, this energy flux is constant with pressure throughout the atmosphere and is represented by the dotted region in **Figure 1**.

At great depths in the interior of a brown dwarf or gas giant, the electron density is high and thermal photons cannot propagate far, so energy transport is dominated by convection. Reviews by Stevenson & Salpeter (1976) and Hubbard & Smoluchowski (1973) discuss this point. At large ages, very massive brown dwarfs can develop small conductive cores (Lunine et al. 1986, Chabrier et al. 2000), but this is far below the atmosphere. Because convection in these dense atmospheres is very efficient, the gradient in the deep thermal temperature profiles, $\nabla = d\log T/d\log P$, is expected to closely follow convective adiabats (i.e., thermal profiles of constant entropy), with $\nabla = \nabla_{\text{ad}}$ (Baraffe et al. 2002). These assumptions can break down if there are composition gradients that impede convection or deep windows in molecular opacity (e.g., Guillot et al. 1994, Leconte & Chabrier 2012), which are eventualities that we ignore here.

Convection delivers thermal energy to/through the base of the atmosphere (represented by the blue-shaded region at large pressures in **Figure 1**), and thermal radiative transport (represented by the orange-shaded region in **Figure 1**) begins to become more important as the atmosphere thins with increasing radius (or decreasing pressure). If there are wavelength regions that both have low opacity and overlap with the local Planck function, then energy can be radiated away through these opacity "windows." At some point, as progressively more energy is carried away from the increasingly tenuous atmosphere by radiation, the temperature profile no longer changes as steeply with altitude, indicating that convection has ceased. Above this level, referred to as the radiative-convective boundary (or RC boundary), energy is carried by radiation, and the atmospheric thermal profile is governed by radiative equilibrium.

In some cases, as the temperature falls with increasing altitude and the peak of the Planck function moves to ever longer wavelengths, this peak may again overlap with a wavelength region of strong opacity. This can again impede thermal radiative energy transport and reinvigorate convection over a small vertical region, called a detached convective zone (see the smaller blue-shaded region at lower pressures in **Figure 1**). **Figure 2** better illustrates the physics of such a situation, showing model profiles of temperature, temperature gradient, and the adiabatic gradient for a cloud-free late T dwarf. For this model case a detached convective region is apparent near
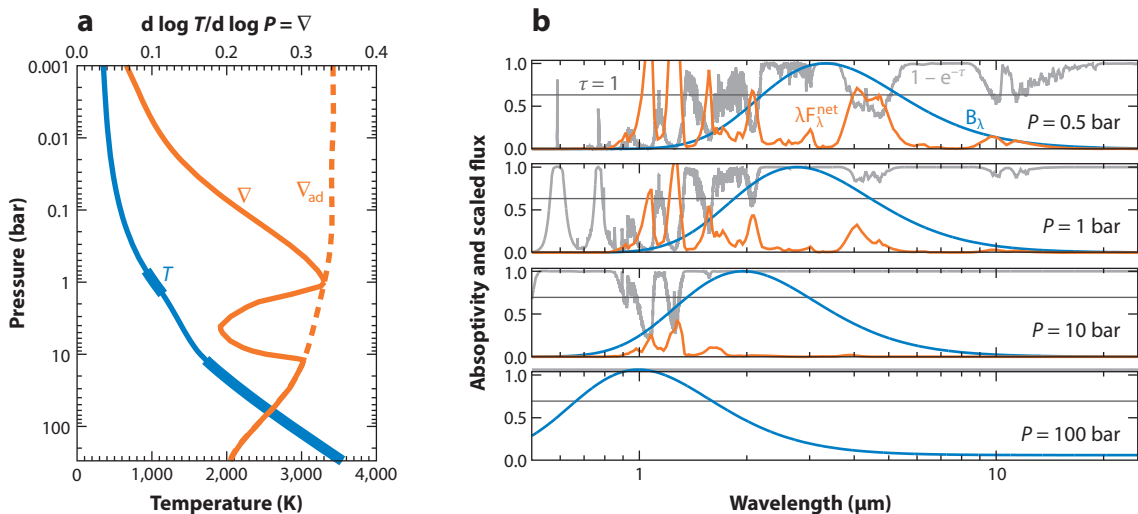
Illustration of some of the influences on a radiative-convective model, as well as model output. (*a*) A computed thermal profile (*blue*) for a cloud-free mid-T dwarf showing temperature as a function of pressure in the atmosphere. Orange curves compare the computed atmospheric temperature gradient (∇, *solid orange line*) with the local adiabatic gradient (∇_{ad}, *dashed orange line*). The model has two convection zones (*thickened blue line*), and in both regions $\nabla = \nabla_{ad}$. (*b*) Illustration of why these two convective zones form—each subplot shows, for the indicated pressure level, spectra of the local Planck function (*blue*), the scaled net thermal flux (*orange*), and the column absorptivity (*dark gray*) (i.e., $1 - e^{-\tau}$, where τ is the optical depth between the top of the atmosphere and the indicated pressure). The absorptivity for $\tau = 1$ is shown as a horizontal line in light gray. In the deepest level ($P = 100$ bar), convection is carrying the internal heat flux, and the net thermal flux is small. However, near $P = 10$ bar, windows in the opacity spectrum between 1–2 μm align with the local Planck function, thus allowing thermal radiation to carry the internal flux, and the atmosphere forms a deep radiative layer. Further up in the atmosphere, at $P = 1$ bar, the local Planck function moves into a region of strong water vapor and methane opacity, thereby reinvigorating convection, which then carries some part of the internal heat flux. Finally, by $P = 0.5$ bar, the atmosphere is in strict radiative equilibrium, which remains toward all smaller pressures (or higher altitudes).

1 bar. For four different pressure levels, spectra of the local Planck function, net thermal radiative flux, and absorptivity of the overlying column of gas are also provided. The detached convective region forms when the peak of the local Planck function overlays strong water vapor and methane absorption bands at 2.7 and 3.3 μm, respectively.

As altitude increases, the atmosphere becomes optically thin to thermal radiation at most wavelengths. However, some strong molecular bands may remain optically thick to fairly high altitudes and will continue to radiate, even while the atmosphere is in general optically thin. For this reason the equilibrium radiative profile is not the same as that expected for a gray atmosphere (i.e., an atmosphere in which the opacity is treated as a wavelength-independent quantity), which reaches a constant-with-altitude "skin temperature" (for a more detailed discussion, see Pierrehumbert 2010, p. 298).

If the atmosphere is irradiated (i.e., receiving energy from a parent star), then thermal radiative transport and convection must carry the internal heat flux as well as the net absorbed stellar flux. In **Figure 1**, this is shown conceptually by the vertically striped flux profile on the right side. For Jupiter, the internal and absorbed incident fluxes are about the same (Hanel et al. 1981). In the case of Uranus the internal flux is small (Pearl et al. 1990), whereas for the so-called hot Jupiters the incident flux dominates completely over the internal contribution.

For a given atmosphere, the internal heat flux and profile of net absorbed stellar flux, along with the opacity structure, control the thermal structure. The equilibrium temperature profile obeys

$$F_t^{net}(P) + F_c(P) + F_\odot^{net}(P) - F_i = 0, \tag{4}$$

where F_t^{net} is the net thermal flux (defined below in Equation 6), F_c is the convective flux, $F_\odot^{net}$ is the net stellar flux, and, as before, F_i is the internal heat flux. Methods for computing these flux profiles, and for determining the thermal structure that satisfies Equation 4, are the focus of this review.

3. RADIATION

A central problem in understanding the equilibrium thermal structure of a substellar atmosphere is to understand energy transport by radiation through the atmosphere. For irradiated bodies, the absorption of stellar flux throughout the atmosphere and/or at the surface drives the climate physics that determine thermal structure. All worlds lose energy by emitting thermal radiation, and thermal radiative transport of energy occurs throughout all atmospheres. In this section, we discuss various aspects of this problem, focusing on expressions for the radiative energy fluxes.

3.1. Radiative Transfer

Heating and cooling by radiative transfer occur as a result of a gradient in the net radiative energy flux,

$$q_r = \frac{g}{c_P} \frac{dF_r^{net}}{dP}, \tag{5}$$

where q_r is the radiative heating rate (in, for example, K s^{-1}), c_P is the local atmospheric heat capacity, and F_r^{net} is the net radiative flux density (typically referred to as just the radiative flux). The net radiative flux is partitioned between an upwelling stream (i.e., toward lower pressures) and a downwelling stream (i.e., toward higher pressures), with

$$F_r^{net} = F_r^+ - F_r^-, \tag{6}$$

where a "+" indicates upwelling and a "−" indicates downwelling. Note that the total radiative heating rate is determined from the bolometric net flux, with

$$F_r^{net} = \int_0^\infty F_{r,\nu}^{net} d\nu, \tag{7}$$

where $F_{r,\nu}^{net}$ is the spectrally resolved net flux. Thus, in the absence of biases in the calculations, uncertainties in the spectrally resolved fluxes at a particular frequency or wavelength can cancel those at other frequencies. However, a common issue for thermal radiative transport models is that, in very opaque regions of the atmosphere, the upwelling and downwelling fluxes approach the same value so that the net thermal flux is calculated as the difference between two typically large and similar numbers, requiring high accuracy in the computation of F_r^+ and F_r^-.

Most radiative transfer models, in one way or another, solve the 1D, plane-parallel radiative transfer equation (RTE),

$$\mu \frac{dI_\nu}{d\tau_\nu} = I_\nu(\tau_\nu, \mu, \phi) - S_\nu(\tau_\nu, \mu, \phi), \tag{8}$$

where I_ν is the spectral radiance, τ_ν is the frequency-dependent extinction optical depth (which increases toward higher pressures), μ is the cosine of the zenith angle, ϕ is the azimuth angle, and S_ν is the source function. Optical depth can be determined from the absorption coefficient (see

Section 6), k_ν (in units of squared centimeters per gram or equivalent), via the differential relation

$$d\tau_\nu = -k_\nu \rho_a dz, \tag{9}$$

where ρ_a is the mass density of the absorber (and absorbers simply combine linearly in $k_\nu \rho_a$). The source function, S_ν, is given by

$$
\begin{aligned}
S_\nu(\tau_\nu, \mu, \phi) =\; & \omega_\nu F_\nu^\odot e^{-\tau_\nu/\mu_\odot} \cdot p_\nu(\tau_\nu, \mu, \phi, -\mu_\odot, \phi_\odot)/4\pi \\
& + (1 - \omega_\nu) B_\nu(T(\tau_\nu)) \\
& + \omega_\nu \int_0^{2\pi} d\phi' \int_{-1}^1 d\mu' \cdot I_\nu(\tau_\nu, \mu', \phi') p_\nu(\tau_\nu, \mu, \phi, \mu', \phi')/4\pi,
\end{aligned}
\tag{10}
$$

where $\omega_\nu = \omega_\nu(\tau_\nu)$ is the frequency-dependent single scattering albedo, $F_\nu^\odot$ is the top-of-atmosphere solar (or, more generally, stellar) irradiance, $\mu_\odot$ is the solar zenith angle, $\phi_\odot$ is the solar azimuth angle, p_ν is the scattering phase function, B_ν is the Planck function, and $T(\tau_\nu)$ is the atmospheric temperature profile. The final term on the right-hand side of Equation 10, which represents scattering from directions (μ', ϕ') into the beam at (μ, ϕ), complicates radiative transfer calculations, as it turns the RTE into an integro-differential equation. Note that in the planetary literature it is common to split radiative transfer calculations into solar/stellar and thermal components, wherein the source function would then omit the second and first terms on the right-hand side of Equation 10, respectively. In the case of hot Jupiters there can be substantial wavelength overlap between the thermal emission and incident flux, although they have very different angular distributions. The upwelling and downwelling fluxes are related to the angle-dependent radiances by

$$
\begin{aligned}
F_\nu^+(\tau_\nu) &= \int_0^{2\pi} \int_0^1 I_\nu(\tau_\nu, \mu, \phi)\mu\, d\mu\, d\phi, \\
F_\nu^-(\tau_\nu) &= -\int_0^{2\pi} \int_{-1}^0 I_\nu(\tau_\nu, \mu, \phi)\mu\, d\mu\, d\phi.
\end{aligned}
\tag{11}
$$

A pair of boundary conditions is needed to solve the RTE, and these typically specify the downwelling radiation field at the top of the model atmosphere and the upwelling radiation field at the bottom of the atmosphere. For irradiated bodies, the top-of-atmosphere boundary condition for incident radiation is simply a direct or diffuse stellar flux, and the bottom-of-atmosphere boundary condition is that either no flux returns from the deep atmosphere or the deep atmosphere has a specified albedo that reflects back some small radiative flux. Thermal calculations assume zero downwelling flux at the top of the atmosphere. The thermal bottom-of-atmosphere boundary condition is less obvious, as the atmospheric column is assumed to be infinitely deep, but models usually take (Mihalas 1970, p. 165)

$$I_\nu(\tau_\nu = \tau_\nu^*, \mu, \phi) = B_\nu\left(T(\tau_\nu^*)\right) + \mu \left.\frac{dB_\nu}{d\tau_\nu}\right|_{\tau_\nu^*} \quad \forall \mu > 0, \tag{12}$$

where the gradient term allows some flux from deeper layers to contribute at the bottom model level (where $\tau_\nu = \tau_\nu^*$), and the factor of μ ensures that near-vertical streams "see" deeper into the atmosphere at the boundary.

3.2. Approaches to Solving the Radiative Transfer Equation

Solving the RTE requires a certain level of parameterization or simplification. Most commonly, techniques are divided into either two-stream or multistream solutions, in which a stream refers to a particular azimuth-zenith coordinate through the atmosphere. Solutions in the two-stream category are more computationally efficient than multistream calculations and offer analytic

GRAY RADIATIVE EQUILIBRIUM

The nonscattering, gray two-stream equations of thermal radiative transfer,

$$\frac{dF_t^+}{d\tau} = D(F_t^+ - \sigma T^4),$$

$$\frac{dF_t^-}{d\tau} = -D(F_t^- - \sigma T^4),$$

where D is the diffusivity factor (i.e., a constant that accounts for the integration of intensity over the hemisphere, with preferred values ranging from 1.5 to 2) and τ is the gray optical depth, which is related to a gray opacity, k, via $d\tau = kdP/g$, can be combined into a single differential equation,

$$\frac{d^2 F_t^{net}}{d\tau^2} - D^2 F_t^{net} = -2D\sigma \frac{dT^4}{d\tau}.$$

For a nonirradiated object with an atmosphere in radiative equilibrium, the net thermal flux is constant and equal to σT_{eff}^4, so that the previous differential equation can be solved to yield the thermal structure,

$$T(\tau)^4 = \frac{1}{2} T_{eff}^4 (1 + D\tau).$$

Given either a database of gray opacities or by making assumptions about the pressure dependence of k, the temperature profile as a function of pressure can be determined. Analytic expressions for the case in which convection is included are derived in Robinson & Catling (2012).

results that can help provide insight into problems. Multistream calculations provide more detailed information about the angular distribution of intensities and, thus, can provide more accurate solutions for radiant fluxes.

Two-stream solutions have roots in early theories of stellar atmospheres (Schwarzschild 1906) and provide techniques for rapidly computing F_ν^+ and F_ν^- (which are the two streams). As discussed by Meador & Weaver (1980), by making assumptions about the scattering phase function and the distribution of intensity in azimuth and zenith angles, the RTE can be simplified to the two-stream equations:

$$\frac{dF_\nu^+}{d\tau_\nu} = \gamma_1 F_\nu^+ - \gamma_2 F_\nu^- - S_\nu^+,$$
$$\frac{dF_\nu^-}{d\tau_\nu} = \gamma_2 F_\nu^+ - \gamma_1 F_\nu^- + S_\nu^-,$$

(13)

where the frequency-dependent γ-coefficients permit scattering from the upwelling stream into the downwelling stream and vice versa, and $S_\nu^{+/-}$ are level-dependent source terms (see the sidebar, Gray Radiative Equilibrium). A critical analysis of the accuracy of different two-stream implementations is also provided by Meador & Weaver (1980) for cases without internal thermal sources.

A widely used approach to solving the two-stream RTE with both solar and thermal sources is provided by Toon et al. (1989) (which regrettably contains numerous typographical errors). These authors describe a numerically stable matrix-based solution to the two-stream problem. Additionally, to more accurately solve for the thermal radiation field in the presence of scattering, Toon et al. (1989) develop an approach called the two-stream source function technique. Using the solution for the two-stream fluxes, direction-independent scattering source functions, $S_\nu^{+/-}$, are determined. These source functions are then used in a multistream calculation, in which the

intensities from the different streams are integrated (i.e., via Equation 11) to more accurately determine the upwelling and downwelling fluxes. The approach is accurate in most cases except in situations with particles that are both high albedo and strongly forward scattering. Thus, the two-stream source function approach represents an efficient middle ground for computing the atmospheric energy balance and thermal profile between strict two-stream solutions and general multistream solutions; it is the approach currently used in the Marley/Saumon brown dwarf and giant planet models (e.g., Marley et al. 2002, 2012; Fortney et al. 2005; Saumon & Marley 2008; Morley et al. 2012).

True multistream solutions seek to solve the full RTE with self-consistent multiple scattering. Such solutions commonly solve the azimuth-independent form of the RTE (Chandrasekhar 1960, p. 15), as aerosol scattering phase functions are typically expressed according to a single angle—the scattering angle. More general techniques have been developed for solving the azimuth-dependent RTE, which are necessary when, for example, the solar/stellar source comes from a particular azimuth and zenith angle (Milkey et al. 1975, Stamnes et al. 1988).

Numerical techniques for determining angle-dependent intensities along a set of discrete zenith angles (representing the streams) in scattering and/or emitting atmospheres/media have been developed in both the planetary and astrophysical literatures. For the latter, the Accelerated Lambda Iteration (ALI) approach (Cannon 1973, Olson et al. 1986, Hauschildt 1992, Hubeny & Lanz 1992) is most common (see also the review by Hubeny 2003). In ALI, the level- and frequency-dependent source function (S_ν) is iteratively adjusted, with each new iteration providing intensities that are increasingly accurate solutions to the RTE. This technique is currently used in the PHOENIX atmospheric models (Allard & Hauschildt 1995, Barman et al. 2001) and in the TLUSTY radiative transfer model (Hubeny & Lanz 1995) implemented in models by Burrows et al. (2002).

Multistream techniques for solving the RTE developed in the Earth and planetary literature include adding-doubling and discrete ordinates. In the former, optically thin, homogeneous atmospheric layers—with given absorbing, emitting, and scattering properties—are combined to form an inhomogeneous atmospheric model (van de Hulst 1963, Twomey et al. 1966). A set of recursive relations, based on the linear interaction of the radiation with a thin layer, is used to compute the intensities within the inhomogeneous model (Hansen 1969, Wiscombe 1976, Evans & Stephens 1991). The discrete ordinates method, originally developed by Chandrasekhar (1960, p. 56), recasts the RTE as a system of ordinary differential equations and uses matrix techniques to find a solution to the system (Stamnes & Swanson 1981). This method is used in the popular, and publicly available, radiative transfer model DISORT (Stamnes et al. 1988, 2000).

4. CONVECTION

Absorption of stellar flux at a planetary surface or deep in the atmosphere of a gaseous world, or the presence of a large internal heat flux, can lead to thermal structures that are unstable to vertical convection. Here, a parcel of gas that is displaced upward would find itself in an environment in which the density is greater than the parcel's internal density, so the parcel would continue to rise (or parcels displaced downward continue to sink). This instability leads to a critical vertical density gradient in an atmosphere, with convection occurring when the gradient is too steep. Using an equation of state, this density gradient can be related to a temperature gradient (or lapse rate), $-dT/dz$, that defines the limit between thermal structures that are convectively stable versus unstable.

Fortunately, modeling convection in brown dwarf and giant planet atmospheres is more straightforward than in the stellar structure literature (e.g., Hansen et al. 2004, chapter 5), because the ideal gas law applies and the convection is, to a good approximation, adiabatic (Baraffe et al.

2002, Ludwig et al. 2006, Freytag et al. 2010). Given these, the criterion for an unstable lapse rate is

$$-\frac{dT}{dz} > \frac{g}{c_P}, \tag{14}$$

or, by including the equation of hydrostatic equilibrium,

$$\nabla = \frac{d \log T}{d \log P} > \frac{R_s}{c_P} = \nabla_{ad}, \tag{15}$$

where R_s is the specific gas constant, which is equal to k_B/m. Thus, for lapse rates larger than the "dry adiabatic lapse rate", g/c_P (or R_s/c_P in $d \log T/d \log P$), a parcel of gas that is perturbed upward continues to rise, meaning that convection would ensue.

It is important to remember that convection does not create or destroy energy—it simply redistributes heat. Thus, convection schemes should be energy conserving. Because lapse rates in a convectively unstable atmosphere are larger than the adiabatic lapse rate, convection works to move heat from deeper atmospheric levels to levels at lower pressures (higher altitudes). In this regard, convection serves to limit the thermal contrast between the deep atmosphere and the radiative-convective boundary.

Approaches to modeling convection (an inherently three-dimensional process) in one-dimensional thermal structure models are varied. Models rooted in the planetary science literature commonly employ an approach called convective adjustment, whereas those derived from astrophysical sources tend to use mixing-length theory. These are discussed in turn below.

4.1. Convective Adjustment

Convection in brown dwarf and giant planet atmospheres relaxes the thermal structure onto an adiabat (Ludwig et al. 2006), so that the structure throughout the convective portion of the atmosphere can be modeled using the dry adiabatic lapse rate (see the sidebar, Dry Adiabatic Lapse Rates and Temperature Gradients). In their simulations of Earth's atmospheric thermal structure, Manabe & Strickler (1964) outlined a straightforward scheme for forcing convectively unstable atmospheric layers onto an adiabat, which these authors called convective adjustment. In this work, radiative heating and cooling rates were used to timestep a model atmosphere toward radiative equilibrium. At each timestep, and proceeding upward from the surface, the lapse rate for each model layer, $|\Delta T/\Delta z|$, was compared with an adiabatic lapse rate. If the layer was unstable, then the temperatures at the top and bottom of the layer were immediately changed, in an energy-conserving fashion, to give the adiabatic lapse rate. An explicit description of this scheme is given by Manabe & Wetherald (1967).

For atmospheres experiencing a substantial amount of condensation, latent heat release causes the lapse rate in the convective portion of the atmosphere to be smaller than the dry adiabatic lapse rate. For example, on Earth the dry adiabatic lapse rate is $g/c_P = 9.8$ K km^{-1}, whereas the actual average lapse rate [according to the U. S. Standard Atmosphere (1976), NOAA-S/T76-1562] in the troposphere is approximately 6.5 K km^{-1}, which is smaller due to water vapor condensation. So, in the original work by Manabe & Strickler (1964), the convective portion of the atmosphere was simply relaxed to the measured lapse rate instead of the dry adiabatic lapse rate.

Of course, for a given background condensable gas, one expects the influence of latent heating in the convective portion of an atmosphere to be less significant at lower temperatures, as cooler temperatures imply smaller amounts of the condensable. The moist adiabatic lapse rate (Satoh 2004, p. 249) captures these physics by accounting for the effects of latent heat release on a

DRY ADIABATIC LAPSE RATES AND TEMPERATURE GRADIENTS

Combining the dry adiabatic lapse rate, $-\mathrm{d}T/\mathrm{d}z = g/c_P$, and the equation of hydrostatic equilibrium (Equation 1), we find the equivalent of the dry adiabat in pressure-space,

$$\frac{\mathrm{d}T}{\mathrm{d}P} = \frac{1}{c_P \rho}.$$

Then, using the ideal gas law to express density in terms of pressure and temperature, we have

$$\frac{\mathrm{d}T}{\mathrm{d}P} = \frac{k_B T}{m c_P P}$$

or

$$\nabla_{ad} = \frac{\mathrm{d}\log T}{\mathrm{d}\log P} = \frac{R_s}{c_P}.$$

Recalling from kinetic theory that the specific gas constant is equal to $c_P - c_v$, where c_v is the specific heat at constant volume and the ratio of specific heats is

$$\gamma = \frac{c_P}{c_v},$$

we can then write the dry adiabat as simply

$$\nabla_{ad} = \frac{\gamma - 1}{\gamma}.$$

Thus, over regions of the atmosphere where the internal degrees of freedom of the gas are roughly constant, the temperature-pressure relationship along a dry adiabat is given by Poisson's adiabatic state equation,

$$T(P) = T_0 \left(\frac{P}{P_0} \right)^{(\gamma-1)/\gamma},$$

where T_0 and P_0 are a reference temperature and pressure, respectively, along the adiabat.

parcel of air that experiences condensation while being lifted adiabatically through the background atmosphere. Whereas multiple species indeed condense in ultracool dwarf atmospheres, in practice the contribution of latent heating is only of first-order importance for water clouds, so we forego a deeper discussion of this issue here.

The strength of the convective adjustment approach is that it is computationally efficient—the thermal structure is simply taken to lie on a dry or moist adiabat. Given this assumed structure, numerical models need only determine the location of the radiative-convective boundary and then ensure that temperature and thermal flux are continuous across this boundary.

Convective adjustment has several notable shortcomings beyond the difficulties associated with condensable gases discussed above. First, convective adjustment may not realistically capture the dynamical response of an atmosphere to vertical motions. Super-adiabatic layers are immediately adjusted onto an adiabat, without regard for any vertical mixing timescales. This assumption is justified when only a steady-state solution is required but could become problematic when studying time-dependent atmospheric variability (see Section 10.1). Additionally, convective adjustment does not straightforwardly predict an eddy diffusion coefficient, which is a critical input to chemistry and cloud models. One potential bypass for this shortcoming is to follow the scaling arguments of Gierasch & Conrath (1985, their equation 16), who use mixing-length theory to derive an expression for the eddy diffusivity.

CONVECTIVE EFFICIENCY

Using the turbulent diffusivity in Equation 18, we can write the convective flux (Equation 17) as

$$F_c = \rho c_P l^2 \left(\frac{g}{T}\right)^{1/2} \left[-\left(\frac{dT}{dz} + \frac{g}{c_P}\right)\right]^{3/2}.$$

If we then assume that the atmospheric lapse rate is a certain fraction larger than the dry adiabatic lapse rate, with

$$\frac{dT}{dz} = -(1+f)\frac{g}{c_P},$$

and that the mixing length is simply the pressure scale height, then the convective flux is

$$F_c = \rho c_P H^2 \left(\frac{g}{T}\right)^{1/2} \left(f\frac{g}{c_P}\right)^{3/2}$$

$$= f^{3/2} R_s P \left(\frac{T}{c_P}\right)^{1/2},$$

where the second step used the ideal gas law and the definition of the pressure scale height. Notably, the gravitational acceleration has cancelled out of this expression.

We can now get a sense for how efficient convection is at returning a superadiabatic lapse rate to near the dry adiabatic value. In the convective region of a mid-L dwarf ($T_{eff} = 1,900$ K, $g = 100$ m s^{-1}), with $P = 10$ bar, $T = 3,500$ K, and $c_P = 10^9$ erg g^{-1} K^{-1}, and with $R_s = 4 \times 10^7$ erg g^{-1} K^{-1}, we find $F_c = 7 \times 10^{11} f^{3/2}$ erg cm^{-2} s^{-1}. This flux is impressively large—even for a 1% deviation from the dry adiabat (i.e., $f = 0.01$), the convective flux is large enough to carry the entirety of the internal heat flux, or $\sigma T_{eff}^4 = 7.4 \times 10^8$ erg cm^{-2} s^{-1}. Thus, even very minor deviations of the lapse rate from the dry adiabatic value will be promptly eliminated.

4.2. Mixing-Length Theory

Mixing-length theory (Prandtl 1925, Vitense 1953, Böhm-Vitense 1958) uses dimensional and scaling arguments to model convective fluxes and has seen successful applications and development in both the astrophysical and planetary science literatures (Henyey et al. 1965, Gierasch & Goody 1968, Spiegel 1971, Castelli et al. 1997). In this approach, convection is modeled as the diffusion of heat through a turbulent medium (see the sidebar, Convective Efficiency). The turbulent diffusivity for heat is taken as

$$K_h = wl, \tag{16}$$

where l is a characteristic length over which turbulent mixing occurs (i.e., the mixing length), and w is a characteristic upward transport velocity. For a parcel lifted adiabatically through l, the temperature difference between the parcel and its surroundings is $\Delta T = -l(dT/dz + g/c_P)$, in which dT/dz is the lapse rate for the parcel such that the convective flux is

$$F_c = w\rho c_P \Delta T = -\rho c_P K_h \left(\frac{dT}{dz} + \frac{g}{c_P}\right), \tag{17}$$

where, of course, a convective heat flux is only present when the atmosphere is unstable to convection (i.e., $-dT/dz > g/c_P$).

Models usually assume that the mixing length is proportional to the pressure scale height, with $l = \alpha H$, where α is a free parameter, typically of order unity [see Burrows et al. (2001), Baraffe et al. (2002), and Robinson & Marley (2014) for exploration of this parameter]. The characteristic

transport velocity can be derived from buoyancy force arguments (Kippenhahn et al. 2012, p. 62), yielding $w = l[-g/T\,(\mathrm{d}T/\mathrm{d}z + g/c_P)]^{1/2}$. Thus, the turbulent diffusivity in a convectively unstable portion of the atmosphere is given by

$$K_b = l^2 \left[-\frac{g}{T}\left(\frac{\mathrm{d}T}{\mathrm{d}z} + \frac{g}{c_P}\right)\right]^{1/2}. \tag{18}$$

Mixing-length approaches benefit from being simple and computationally efficient. Additionally, these techniques directly compute the convective heat flux and turbulent diffusivity (Equations 17 and 18, respectively). The latter gives information about mixing processes in the convective portion of the atmosphere and can be used in chemical and aerosol transport models. Also, because convective heating and cooling rates can be computed from the convective flux profile, mixing-length models can be used to study time-dependent atmospheric processes and phenomena.

A common criticism of mixing-length theory is that the mixing length, l, is ambiguous. Additionally, the theory does not directly predict the thermal structure in the convective regime (unlike convective adjustment, which imposes the adiabat) but, instead, must solve for the thermal structure using the relevant fluxes and heating rates.

4.3. Beyond One-Dimensional Models of Convection

Studies of stellar structure and work in the Earth and planetary sciences have benefited from two- and three-dimensional modeling of convection and from comparing these models with one-dimensional methods for simulating convection. For example, Chan et al. (1982) performed two-dimensional simulations of turbulent convection in the deep atmospheres of stars and noted that the vertical velocities in their models were correlated over a characteristic length comparable with the pressure scale height, which lends some support to the mixing-length picture outlined above. Cattaneo et al. (1991) used three-dimensional models to study convection in an astrophysical setting and noted that local mixing-length theories can adequately represent the turbulent transport of energy.

The brown dwarf and irradiated giant planet literature has seen very little development of convection-resolving models. Freytag et al. (2010) presented local box models of small-scale convection and studied its impact on dust transport at scales of hundreds of kilometers. Showman & Kaspi (2013) presented global models of large-scale convection and its interaction with atmospheric circulation, and Zhang & Showman (2014) presented global circulation models of the stratified atmosphere. Application of models and techniques from the Earth, planetary, and stellar literatures may, then, prove fruitful in advancing our understanding of convection in brown dwarf and giant exoplanet atmospheres. An extensive review of the dynamics of hot exoplanet atmospheres has recently been provided by Heng & Showman (2014).

5. CHEMISTRY

In addition to convection and radiative transfer, of course, a key characteristic of an atmosphere is its chemical make-up, which can in turn affect the computation of the thermal structure as gas abundances influence many processes (such as, e.g., opacities and, thus, radiative energy transport). In this section, we briefly review influences on gas concentrations and discuss how the atmospheric composition is computed in the context of one-dimensional modeling. More extensive reviews of this topic have been conducted by Lodders & Fegley (2006) and Burrows et al. (2001).

5.1. Abundances

Of central importance to modeling the chemistry throughout a brown dwarf or giant planet atmosphere are the abundances of the underlying elements that make up the more complex molecules that form in these atmospheres. These abundances are affected by two key processes. First, the overall elemental abundances for the object determine the baseline distribution of elements. Second, the formation and rainout of condensates influence the availability of certain elements, possibly starving upper atmospheric layers (i.e., those at lower pressures and cooler temperatures) of certain elements.

5.1.1. Elemental. A key assumption in any atmosphere model is the underlying elemental abundances. The most important abundances are those of carbon and oxygen (C and O), as H_2O, CO, and CH_4 are key absorbers whose concentrations are controlled by the availability of C and O. Abundances are typically referenced to those of the Sun, and an assumption of "solar abundances of the elements" is usually the starting point for atmospheric modeling. Asplund et al. (2009) review the challenges in defining such an abundance set. Unfortunately the solar C and O abundances are uncertain, and the generally accepted values have varied with time, even over the short history of ultracool dwarf modeling (e.g., Anders & Grevesse 1989, Allende Prieto et al. 2001, 2002, Asplund et al. 2009, Caffau et al. 2011). For this reason any model comparison between different modeling groups must begin with a comparison of the assumed elemental abundances. Barman et al. (2011), for example, use the abundances of Asplund et al. (2009), which are very similar to the Lodders (2003) abundances utilized by the Marley/Saumon group.

Not all atmospheres have solar abundances of course. Individual brown dwarfs or giant planets sport a variety of compositions, and the defining characteristic of extrasolar giant planets may well be atmospheric abundances that depart from that of their primary stars. Thus any given atmosphere model must make some choice for the initial elemental abundances.

An additional important aspect of abundance determination is the C/O ratio, which affects the relative abundance of not only the major C- and O-bearing species but other compounds as well. As the C/O ratio increases toward unity, the condensation temperatures of oxides and silicates fall, and C-bearing compounds become more prevalent [see discussion by Lodders (2003) and references therein]. Indeed the accepted "solar" value of C/O has ranged from 0.4 to 0.6 and is known to vary among other stars (for a recent discussion, see Fortney 2012). Thus the assumed model C/O ratio should also always be noted when presenting modeling results. Fortney (2012) has suggested that brown dwarf spectra are especially well-suited to measuring the C/O ratio in the Solar Neighborhood. In the extreme case, if a brown dwarf were to be formed with atmospheric C/O > 1, the entire atmospheric chemistry would be grossly altered in the L dwarf regime, with essentially all available O going to form CO instead of H_2O and the excess C forming C_2H_2, HCN, and other reduced hydrocarbons and nitriles. However, no such brown dwarfs have yet been found, and we neglect this possibility here.

5.1.2. Rainout. A crucial distinction among modeling approaches arises in the treatment of the chemistry of condensates. Once a condensate is formed, two limiting cases can be imagined (Lewis 1972). In one case the solid grain or liquid drop continues to chemically interact with the surrounding gas to arbitrarily low temperatures. This is a description of "true" chemical equilibrium in which a given initial set of elements is always assumed to be in chemical equilibrium at a specified temperature and pressure. This assumption was explored by Burrows & Sharp (1999) and is implicit in the COND and DUSTY models (Chabrier et al. 2000, Allard et al. 2001). In the other extreme, the condensate can be imagined to rain out of the atmosphere, precluding further

reactions with the neighboring gas, a limit sometimes called rainout chemistry (although sedimentation chemistry is probably a better phrase, rainout has become ingrained in the literature).

Rainout and the gas and cloud chemistry in substellar atmospheres are discussed by Lodders (1999, 2004), Burrows & Sharp (1999), and Lodders & Fegley (2006). An important consequence of the rainout chemistry is that reactions that would be expected to take place between condensed species and the gas at temperatures cooler than the condensation temperature are excluded. For example, without the rainout assumption, iron grains would react with H_2S gas to form FeS, thus removing H_2S from the atmosphere at around 500 K. In contrast, under the rainout assumption the iron grains are presumed to fall out of the atmosphere after they form at around 2,000 K, thereby precluding further reaction with H_2S, which then stays in the gas phase. Because H_2S is indeed observed in Jupiter's atmosphere, this is presumably the correct limit (Barshay & Lewis 1978, Fegley & Lodders 1994, Niemann et al. 1998).

Another example of the importance of rainout arises in the alkali chemistry and the interaction of the alkali metals with silicate grains that initially form around 1,800 K. Without the rainout assumption, gaseous sodium and potassium undergo a series of reactions with these grains that ultimately produce alkali feldspar ($[Na,K]AlSi_3O_8$), thereby removing Na and K from the gas at around 1,400 K. With rainout the silicate grains that form near 1,800 K fall, do not react with the atmosphere at cooler temperatures, and alkali feldspar does not form (Lodders 1999). In this limit sodium remains in the atmosphere until about 700 K at which point Na_2S and KCl form. Marley et al. (2002) argue that the far red optical spectra of T dwarfs support the rainout hypothesis. More recently, Morley et al. (2012) convincingly demonstrate the presence of such alkali condensates in cool T dwarf spectra. Taken together these lines of evidence support the rainout limit.

5.2. Equilibrium Chemistry

Given an abundance of all relevant elements and appropriate thermodynamic data, the abundances of gaseous species at any pressure and temperature can be computed. Different groups use one of primarily two different methods for solving for the gas abundances in chemical equilibrium. The quality of the results ultimately depends upon the number of species considered and the veracity of the underlying thermodynamic data, which are not always available for all reactions and species of interest.

The two methods for finding equilibrium are commonly termed mass action and Gibbs minimization. The mass action approach utilizes the equilibrium constants for all relevant chemical reactions, as well as mass conservation, to find the abundance of each molecule and condensate of interest at a given pressure and temperature. Gibbs minimization solves for the mixture of species that has the lowest Gibbs free energy, given the pressure, temperature, and assumed elemental abundances. With identical thermodynamic data—and the same assumptions regarding rainout—the two approaches should give identical results. However, in practice, typically because of computational limitations, mass conservation is not always achieved by Gibbs minimization methods. Computational considerations also often limit the number of elements and compounds that can be included in this approach. van Zeggeren & Storey (1970) provide the best source for learning about the details of chemical equilibrium calculations.

For specific application to brown dwarf atmospheres, we refer readers to Sharp & Burrows (2007, their section 4), who provide ample discussion and examples of the free-energy minimization procedure. Likewise, the mass action approach is described by Fegley & Lodders (1994) in the context of Jupiter's atmosphere, and the method has been used to study the chemistry of the major elements in brown dwarf and exoplanet atmospheres by Lodders & Fegley (2002) and Visscher et al. (2006).

Regardless of the method employed, the curation and vetting of relevant thermodynamic data are time-consuming processes. For example, Lodders, Fegley, and collaborators follow approximately 2,000 gaseous and 1,700 solid or liquid species in their code. Construction of the relevant thermodynamic database poses a substantial "barrier to entry" for new scientists interested in computing their own atmospheric chemistry.

Examples of equilibrium gas abundances, or ratios of gas abundances, for several key species of interest [from rainout models by Lodders & Fegley (2002) and Visscher et al. (2006)] are shown in **Figure 3**, along with model temperature profiles for a few representative objects. The effects of condensation removing Ti and Fe can clearly be seen. Also, the ratios of the concentrations of CH_4 to CO and NH_3 to N_2 demonstrate the preferred chemical state of C and N at any given temperature and pressure.

5.3. Disequilibrium Chemistry

Although Jupiter's atmosphere is primarily in the expected state of chemical equilibrium, its atmospheric composition departs from equilibrium in some important respects, and these provide a guide for understanding similar excursions in brown dwarf and exoplanet atmospheres. First, convection is known to mix CO from the deep atmosphere, where it is the favored carbon-bearing species, up to the observable atmosphere, where CH_4 should be overwhelmingly dominant (Prinn & Barshay 1977, Bézard et al. 2002). This can happen in situations in which the mixing time for species to be transported by convection is shorter than the timescale for a species to come into chemical equilibrium with its surroundings.

Because carbon is tied to oxygen by a strong triple bond in CO, it can be difficult for atmospheric chemical processes to convert the species to methane, even when this would be thermodynamically favored. **Figure 4** illustrates the somewhat tortuous chemical pathway linking CO to CH_4. For this reason Fegley & Lodders (1996) predicted that CO would be discovered in the atmospheres of what were then termed the methane dwarfs (now the T dwarfs) and, indeed, several observational studies (Noll et al. 1997, Oppenheimer et al. 1998, Saumon et al. 2000, Geballe et al. 2009) found excess CO in these objects. Likewise, excess CO was found in the atmospheres of the cooler transiting planets, and the repeated "discovery" of chemical disequilibrium became, for a while, something of an industry within the exoplanet community.

The efficiency with which CO can be transported upward depends upon both the vigor of eddy mixing and the chemical equilibrium timescale. The former is usually parameterized in models with K_h, the eddy diffusivity for heat discussed earlier, whereas the latter depends upon the details of the chemical pathway. The usual approximation used in modeling this process is that the atmospheric abundance of CO is fixed at the point at which the chemical equilibrium timescale is equal to the mixing timescale, commonly known as the quench approximation (e.g., Fegley & Lodders 1996, Saumon et al. 2000, Lodders & Fegley 2002, Hubeny & Burrows 2007; see the sidebar, Quenching). An example is shown in **Figure 5**. For this model a pure equilibrium calculation would find that C in the atmosphere should be almost entirely in the form of methane above approximately 1 bar when the thermal profile has entered in the methane stability field. However, in the presence of vertical mixing, CO is transported upward and can be the dominant species when mixing is vigorous. The most comprehensive discussions of this process are provided by Hubeny & Burrows (2007) and Zahnle & Marley (2014).

Zahnle & Marley (2014) review the disequilibrium mixing literature and argue that quenching is more gravity-dependent than previously recognized. They suggest that, in the lowest-mass extrasolar planets, such as those that are expected to be discovered by the Gemini Planet Imager (GPI) and the Spectro-Polarimetric High-contrast Exoplanet REsearch (SPHERE) surveys for
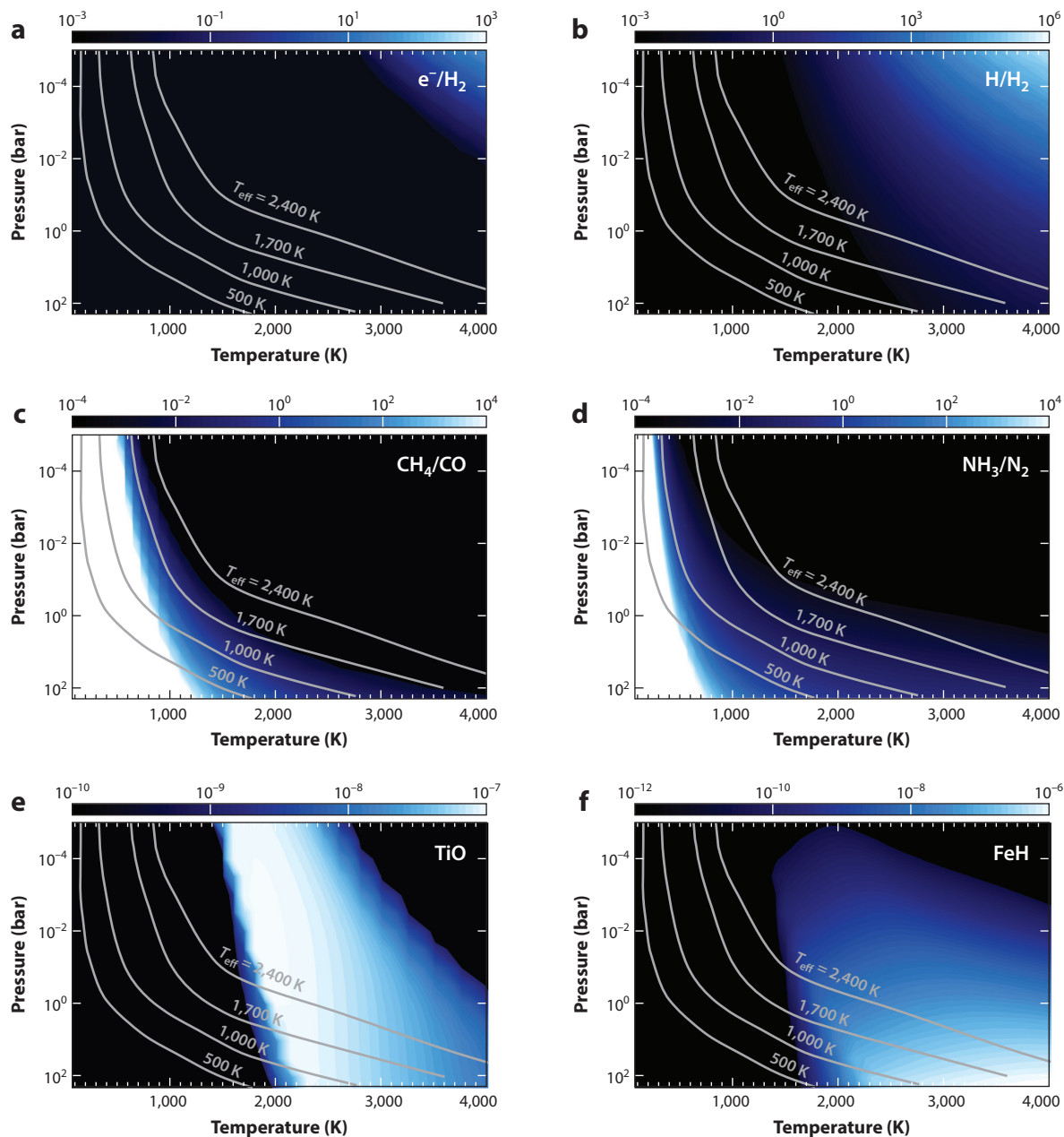
Figure 3

Abundances or ratios of abundances for various species of interest, as a function of pressure and temperature, from Lodders & Fegley (2002) and Visscher et al. (2006). Species are listed in the upper-right of each subplot, and the abundance, or abundance ratio, is according to the color bar at the top of each subplot. Thermal profiles from cloud-free models of various effective temperatures, and with $g = 10^3$ m s^{-2}, are overplotted in gray. Photospheres for these models typically extend to depths of 3–30 bar. Note the transition from CO to CH$_4$ at cooler temperatures and a similar transition for N$_2$ to NH$_3$. Both TiO and FeH are strongly depleted by rainout at lower temperatures.
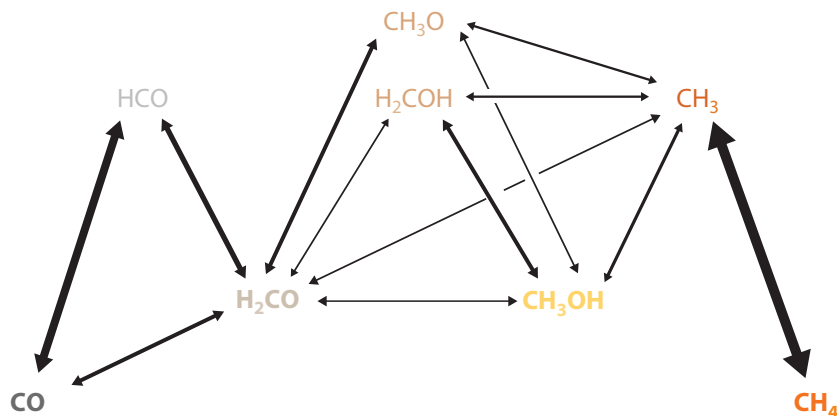
Figure 4

Major chemical pathways linking CO and CH_4 in an H_2-rich atmosphere (from Zahnle & Marley 2014). Reactions from left to right are with H_2 or H. Key intermediate molecules are formaldehyde (H_2CO) and methanol (CH_3OH), whereas other intermediates (HCO, H_2COH, CH_3O, CH_3) are short-lived free radicals. The vertical position of individual species gives a rough indication of the energetics. Energy barriers correspond to breaking C-O bonds—from triple to double, from double to single, and from single to freedom. Relative magnitudes of reaction rates are indicated by arrow thickness. Conceptually, higher temperatures and lower pressures tilt the plot as a whole to the left, with carbon pooling in CO. Lower temperatures and higher pressures tilt the plot as a whole to the right, and carbon pools in CH_4.

young planets (Beuzit et al. 2008; Macintosh et al. 2008, 2012), CO may be the dominant C-bearing species until temperatures as low as approximately 600 K. Furthermore, CO is not the only species that can be in disequilibrium because of mixing. Similar arguments apply to the equilibrium between N_2 and NH_3, as well as the chemistry of PH_3 and GeH_4. Indeed signs of NH_3 underabundance compared with the expectations of equilibrium chemistry have already been reported in brown dwarfs (Saumon et al. 2006), which has also been reviewed by Zahnle & Marley (2014).

One final important disequilibrium process should be noted—under the presence of incident UV radiation, methane, hydrogen sulfide, and other species may be photochemically destroyed, leading to the creation of more complex molecules. In cool Solar System atmospheres the resulting species often form haze particles, which themselves become important opacity sources. A thorough post-*Voyager* review of methane photochemistry in the context of giant planets is conducted by Bishop et al. (1995), whereas an informative overview of giant planet C, N, O, and S photochemistry is discussed by Moses (2000). Zahnle et al. (2009) consider photochemical processes that are unique to giants much warmer than Jupiter, specifically studying sulfur photochemistry in hot Jupiter atmospheres. In general, photochemistry in any giant more heavily irradiated than Jupiter will be much more complex than in Solar System giants because species that are usually trapped in tropospheric clouds, such as NH_3, H_2S, and H_2O, should instead be present in the upper atmosphere where the incident UV flux is far higher.

6. GAS OPACITY

The transition from hot, atomic, continuum-opacity-dominated, solar-like stars to the cool, mostly neutral, and molecular atmospheres of the late M, L, T, and Y dwarfs is nowhere more apparent

QUENCHING

Turbulent motions will tend to cause the vertical mixing of chemical species throughout an atmosphere. Chemical disequilibrium can be established if mixing supplies a species to an atmospheric level faster than the local chemical reactions can remove it. The concentration of the species is then locked into its value from deeper in the atmosphere, in a process called quenching. The quenching level is roughly where the mixing timescale equals the chemical loss timescale, or $t_{mix} = t_{chem}$.

Given the characteristic turbulent velocity, w, mixing over a pressure scale height, H, occurs at a timescale

$$t_{mix} = \frac{H}{w} = \frac{H^2}{K_h},$$

where the second step used Equation 16 with $l = H$ (but see Smith 1998 for an alternative approach to the use of H as well as the discussion in Zahnle & Marley 2014). The value of K_h can either be evaluated from a thermal structure model using mixing-length theory (Section 4.2) or be simply specified as a constant. Above the convective region, the eddy diffusivity from convective mixing is formally zero, but other processes can still drive mixing (e.g., gravity waves), as have been studied for the Solar System planets and brown dwarfs (e.g., Bishop et al. 1995, Freytag et al. 2010).

Chemical loss timescales are more difficult to specify. As reviewed by Zahnle & Marley (2014), one option is to determine the loss timescale by associating it with the rate-limiting step in the loss reaction (although determining this step can be difficult). Alternatively, gridded results from a large suite of photochemical models can be used to determine a functional form of t_{chem}. This approach was adopted by Zahnle & Marley (2014), who propose using an Arrhenius-like rate,

$$t_{chem} = A P^{-b} [M/H]^{-c} e^{B/T},$$

where [M/H] is the metallicity, and A, B, b, and c are coefficients of the fit. For the CO-CH$_4$ system, these authors find

$$t_{chem} = 1.5 \times 10^{-6} P^{-1} [M/H]^{-0.7} e^{42,000/T} \text{ s}.$$

than in the opacities that must be considered to model these atmospheres. Properly accounting for the molecular opacity of key atmospheric constituents is a major task of cool atmosphere modeling. This section reviews the important gaseous opacities in cool atmospheres, focusing on the treatment of molecular absorption lines. Techniques for solving the RTE given a complex spectrum of gas opacities are also discussed.

6.1. Line Strengths and Shapes

Each molecular absorption band is formed from a collection of individual absorption lines, as shown in **Figure 6**, with each line marking a transition in the coupled rotational-vibrational energy state of the molecule. The shapes and strengths of these lines depend on a number of processes, including structural properties of the molecule as well as the local atmospheric conditions in which the line is formed.

In general, an individual spectral line is described by three key parameters—the line position (i.e., the frequency or wavenumber at line center, ν_0, typically in units of cm^{-1}), the line strength [$S = S(T)$, in units of cm^2 molecule^{-1} cm^{-1} or equivalent], and the line shape function [$f(\nu - \nu_0)$, in units of 1/cm^{-1}]. The frequency-dependent absorption coefficient for the line, k_ν, is then expressed
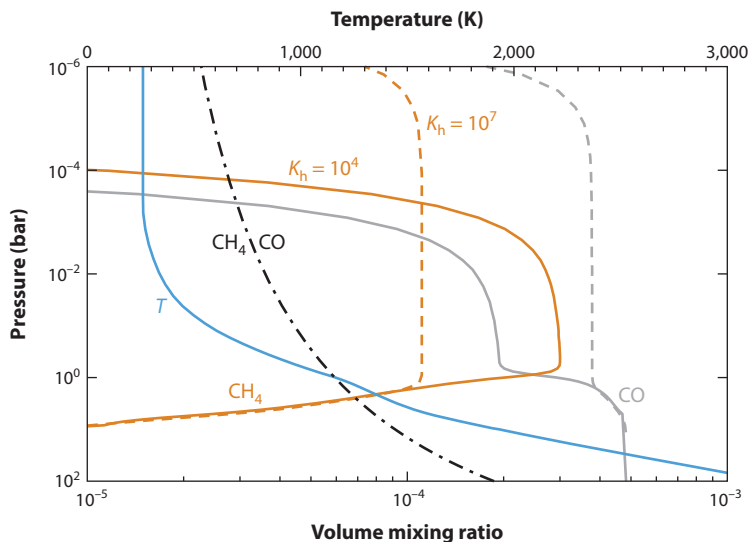
Figure 5

An example of CH_4 and CO disequilibrium. This ~ 2 M_J giant planet model is cloud free, has $T = 600$ K, $g = 10$ m s^{-2}, and no insolation. The P-T profile of the atmosphere (*blue*) is compared with the P-T curve (*dash-dotted black line*) in which the mixing ratios of methane and carbon monoxide are equal under equilibrium conditions. Methane is thermodynamically favored when T is to the left of this curve. Disequilibrium CO (*gray*) and CH_4 (*orange*) mixing ratios, computed by Zahnle & Marley (2014), with $K_h = 10^4$ cm^2 s^{-1} (*solid lines*), and $K_h = 10^7$ cm^2 s^{-1} (*dashed lines*) are shown. Below the quench points, CO and CH_4 are in equilibrium. Above the quench points, the CO and CH_4 mixing ratios are constant with altitude until molecular diffusion leads to the separation of CO and CH_4 from the background H_2 gas at lower pressures.

as

$$k_\nu = Sf(\nu - \nu_0), \tag{19}$$

where the line shape function is normalized such that

$$\int_{-\infty}^{+\infty} f(\nu - \nu_0)d\nu = 1. \tag{20}$$

Thus, the integrated area under an individual line is constant (equal to S), so that broader absorption lines increase opacity in line wings at the expense of opacity near line center.

Large databases, usually referred to as line lists, compile the necessary information for computing absorption line spectra. These databases are based on either lab measurements or quantum chemistry simulations. As a number of line parameters depend on temperature, line lists are typically referenced to a standard temperature (e.g., 296 K). Commonly used line lists include the HITRAN (Rothman et al. 1987, 2013), HITEMP (Rothman et al. 1995, 2010), and ExoMol (Tennyson & Yurchenko 2012) databases; HITEMP is most appropriate for the range of temperatures encountered in substellar atmospheres but only includes data for H_2O, CO_2, CO, NO, and OH. Sources of line lists for more exotic species, and discussion of how to implement these databases, are reviewed and/or tabulated in several recent papers (Sharp & Burrows 2007; Freedman et al. 2008, 2014; Lupu et al. 2014).
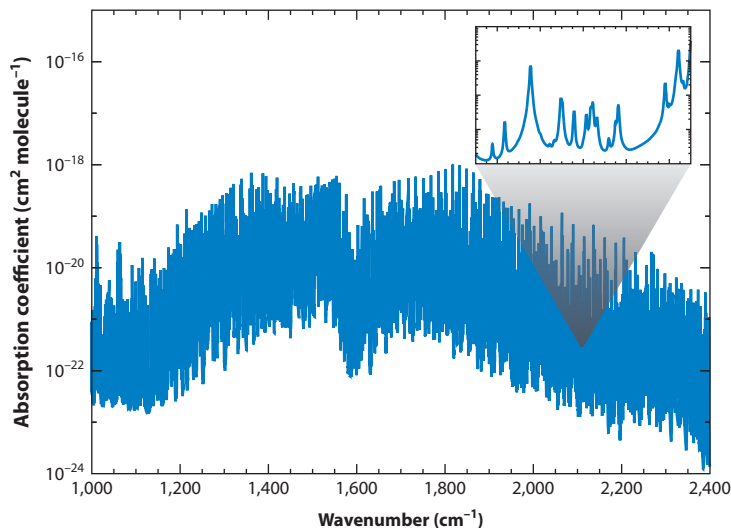
Figure 6

Demonstration of molecular line absorption opacity. Absorption coefficients for the 1,600-cm^{-1} (6.3-μm) water vapor absorption band are shown for a temperature of 1,000 K and a pressure of 1 bar. Inset shows a smaller range, centered at 2,100 cm^{-1} and spanning 10 cm^{-1}, in which individual absorption lines can clearly be distinguished.

Given a line strength S_0, defined at a standard temperature T_0, the temperature-dependent line strength can be computed from (McClatchey et al. 1973)

$$S(T) = S_0 \frac{Q(T_0)}{Q(T)} \exp\left[\frac{E''}{k_B}\left(\frac{1}{T_0} - \frac{1}{T}\right)\right] \frac{1 - \exp(-hc\,v_0/k_B T)}{1 - \exp(-hc\,v_0/k_B T_0)}, \qquad (21)$$

where Q is the internal molecular partition function for vibrational and rotational states, E'' is the lower energy level for the rotational-vibrational transition (commonly supplied in line lists), c is the speed of light ($c = 2.998\times10^{10}$ cm s^{-1}), and h is Planck's constant ($h = 6.626\times10^{-27}$ erg s). The exponential term in the middle of this expression is the familiar Boltzmann distribution for energy states. Standard methods exist for computing partition functions (e.g., Gamache et al. 1990), which describe the temperature-dependent partitioning of rotational-vibrational energy states. The combination of the Boltzmann factor and the partition function weight the line strength by the probability of finding molecules of a given energy state within the ensemble of all states. Finally, the ratio of terms at the end of this expression corrects for stimulated emission, in which a molecule is de-excited from the higher energy state ($E'' + hc\,v_0$) via an interaction with a photon of energy $hc\,v_0$, thereby giving off two photons with the same energy as the initial photon. Viewed as negative absorption, stimulated emission makes the overall strength of the absorption line slightly smaller.

The line shape depends critically on temperature, pressure, and atmospheric composition through so-called foreign broadening. At lower pressures, in which molecular collisions are relatively infrequent, line broadening is dominated by Doppler effects from thermal motions, which has a characteristic Gaussian line shape function,

$$f_D(v - v_0) = \frac{1}{\alpha_D}\sqrt{\frac{\ln 2}{\pi}} \exp\left[-\frac{\ln 2\,(v - v_0)^2}{\alpha_D^2}\right], \qquad (22)$$

where α_D is the Doppler line half-width at half-maximum (HWHM), given by

$$\alpha_D = \frac{v_0}{c}\sqrt{2\ln 2\frac{k_B T}{m}}, \qquad (23)$$

where m is the molecular mass. Thus, Doppler broadening is more effective at higher temperatures and for low-mass molecules, which stem from an assumed Maxwellian distribution of molecular speeds. Some atmospheric models, most notably the PHOENIX models (Allard & Hauschildt 1995, Barman et al. 2001), combine the thermal velocity with a microturbulent velocity that is taken to scale with the convective velocity w (see Section 4.2) (Husser et al. 2013). Physically, this scaling represents a turbulent cascade from the macroscale to the microscale, which broadens individual absorption lines. These velocities are typically of order 1 km s^{-1} that, as an example, is comparable with the gas kinetic velocity of water vapor molecules at roughly 1,000 K. In practice, the microturbulent velocity has been used as a parameter to better reproduce observed spectra and to account for incomplete line lists (Kurucz 1996).

Deeper in the atmosphere, at pressure levels from which most thermal emission spectra emanate, line broadening is dominated by molecular collisional effects on emission and absorption. The line shape for so-called pressure broadened lines is typically taken as a Lorentzian function,

$$f_L(v - v_0) = \frac{1}{\pi}\frac{\alpha_L}{(v - v_0)^2 + \alpha_L^2}, \qquad (24)$$

where α_L is the pressured-broadened HWHM. Typically α_L is computed from a width parameter, γ, obtained from a line list, where

$$\alpha_L = \gamma P \left(\frac{T_0}{T}\right)^n, \qquad (25)$$

where n is a temperature-dependence exponent, also commonly supplied in line lists. The width parameter is different for self-broadening, in which collisions are from molecules of the same species as the absorber, versus foreign-broadening, in which other species dominate the molecular collisions. In some cases, most notably for H_2O in Earth's atmosphere and CO_2 in Venus' atmosphere, the Lorentzian line shape has been found to either overestimate or underestimate absorption in the far wings of pressure-broadened lines. In these situations, it is common to apply a line shape correction, called a χ-factor, to best reproduce the observed data (see, e.g., Winters et al. 1964, Fukabori et al. 1986, Pollack et al. 1993, Meadows & Crisp 1996, Mlawer et al. 2012).

Of course, there are large portions of the atmosphere in which lines are influenced by both Doppler and pressure broadening. Here, a convolution of the line shapes for these two processes is used, called the Voigt line shape, which is given by

$$f_V(v - v_0) = \frac{\alpha_L}{\pi^{3/2}}\int_{-\infty}^{+\infty}\frac{\exp(-y^2)}{(v - v_0 - \alpha_D \cdot y)^2 + \alpha_L^2}\,dy. \qquad (26)$$

Schreier (2011) discusses efficient methods for computing this expression. **Figure 7** compares line shapes for Doppler broadening (both with and without a microturbulent velocity), pressure broadening, and the combination of these into a Voigt line shape.

An important source of uncertainty in opacity calculations is that the width parameter and the temperature-dependence exponent are usually measured for terrestrial air as the broadening gas and are expected to have different values when other gases (e.g., H_2) are the primary sources of pressure broadening. Pressure broadening parameters for either H_2 or $H_2 + He$ as the background gas are available for a limited set of molecules and do not typically span a wide range of wavelengths (Bulanin et al. 1984; Le Moal & Severin 1986; Margolis 1993, 1996; Brown & Plymate 1996; Gamache et al. 1996; Gabard 2013). These data are commonly extrapolated to cover the full range
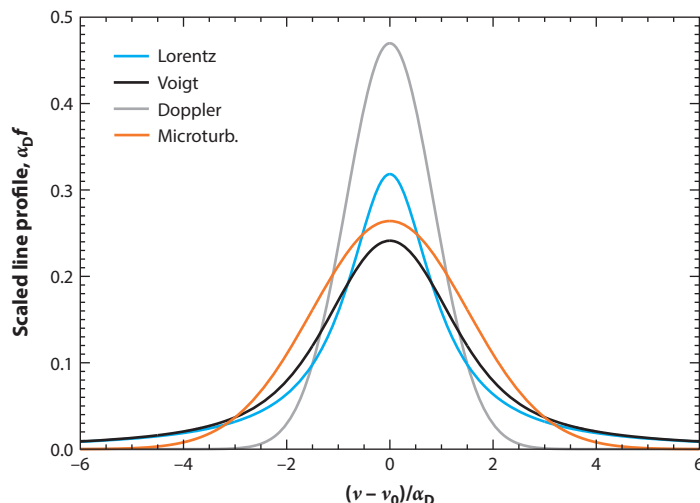
Figure 7

Comparison of different line shapes. The horizontal axis is in units of the Doppler half-width (α_D), so that a half-width of one occurs at unity along the *x*-axis. The line shape, *f*, is scaled by the Doppler half-width, and the Lorentz and Voigt line shapes use $\alpha_L = \alpha_D$, so that the area under each curve is the same (see Huang & Yung 2004). Also shown is a Doppler line shape in which microturbulent broadening is included, where the turbulent velocity is taken to be 1 km s^{-1}.

of wavelengths of interest. When broadening parameters are only available for terrestrial air, width parameters and temperature-dependence exponents are sometimes adjusted by a constant factor derived from insight and a limited set of available data.

Additionally, the power-law temperature dependence in the expression for the Lorentz HWHM likely does not hold over a wide range of temperatures. This is especially problematic for astrophysical applications in which the physical environment is typically quite different from the laboratory conditions where line parameters are measured. Thus theoretical modeling of line shape parameters is commonly employed, in which a wide range of combinations of temperatures, pressures, and broadening gases can be investigated (Gabard 2013, Gamache & Lamouroux 2013).

Even though most of the theory outlined above is straightforward, issues arise owing to the scope of the problem. Line lists can contain more than 10^9 or even 10^{10} transitions, which makes assembling opacities computationally expensive. Efficiency can be gained by omitting weak lines from opacity calculations, which is most effective when gas concentrations are known (or can be estimated) a priori. Additionally, it isn't feasible to sum the contributions from such large numbers of lines out to arbitrarily large distances from line centers. Thus, line shape profiles are commonly truncated at some distance from line center, which necessitates a rescaling of the line shape to maintain the normalization of Equation 20, thus preserving the integrated line strength (Sharp & Burrows 2007).

Finally, whereas the basic procedure for applying molecular opacity databases to atmospheric modeling problems can be easily outlined, there are many subtleties (for example, detailed choices about line broadening, or recognizing errors, which are not uncommon, in the databases). Decision making in these cases benefits from deep experience in the construction and use of line databases. However, relatively few young astronomers specialize specifically in the study of molecular opacity issues, and this lack of new talent may represent a problem for the field in the future.

6.2. Alkali Opacity

At the time of the first T dwarf discoveries, a major shortcoming of the T dwarf models was that they predicted far too much flux in the far red (∼900 to 1,000 nm) compared with observations. One early suggested solution even relied upon a high-altitude, scattering haze to account for the discrepancy (Griffith et al. 1998). In fact the missing opacity source was soon found to be the highly pressure-broadened wings of resonant Na and K lines (Burrows et al. 2000).

Correctly computing the opacity of resonant alkali lines is not straightforward, and mismatches between models and data near 1,000 nm are commonly attributed to shortcomings in the treatment of these lines. Recent work by Allard et al. (2012) on these line shapes should improve the situation, but there are many subtleties in the use of the theoretical results, and there is clearly room for more study of the alkali opacities.

6.3. Continuum Gaseous Opacities

In addition to line and molecular opacities, there are several continuum opacity sources that must be considered. Foremost among these is the collision-induced absorption (CIA, sometimes termed pressure-induced absorption) opacity arising from transitions within supramolecules transiently created during collisions of H_2 molecules with other other gas species, predominantly H_2 and He. From the uncertainty principle, because collision timescales are very short, energy-level transitions within the short-lived supramolecules are not sharply defined, and the resulting opacity is generally smoothly varying with wavelength. A recent compendium has been published by Richard et al. (2012).

Although electron densities are generally quite low in these atmospheres (**Figure 3**), continuum opacity sources associated with free electrons must be accounted for. These include bound-free absorption by H and H^- and free-free absorption by H, H_2, H_2^-, and H^- (see Lenzuni et al. (1991)), as well as electron scattering.

Finally, Rayleigh scattering in the gas is also important for problems involving incident starlight. Rigorous calculations also account for Raman scattering, an important process in the UV for giant planet atmospheres (Pollack et al. 1986).

6.4. Opacities and the Radiative Transfer Equation

As discussed by Goody & Yung (1989, p. 125), radiative calculations involve four distinct scales of wavelength variation: the scale at which the Planck function varies, the scale of gas rotational-vibrational absorption bands, the scale of individual absorption lines, and, most finely, the monochromatic scale at which the absorption coefficient can be considered to be constant. Techniques exist for averaging wavelength-dependent atmospheric opacities across this full range of scales, with the purpose of increasing the speed at which net radiative heating rates can be determined.

6.4.1. Gray opacities. Early studies of the structure and evolution of brown dwarfs (Lunine et al. 1986, 1989) and recent analytic models of the thermal structure of irradiated planetary atmospheres (Hansen 2008, Guillot 2010, Robinson & Catling 2012, Parmentier & Guillot 2014) have used opacities averaged over the entire spectral range, or gray opacities, combined with the gray two-stream equations (e.g., Andrews 2010, p. 84), to compute thermal fluxes in substellar atmospheres. Typically either the Planck mean opacity, k_P, or the Rosseland mean opacity, k_R,

are used, whose averaging are defined, respectively, by

$$k_P(P, T) = \frac{\int_0^\infty k_\nu(P, T) B_\nu(T) d\nu}{\int_0^\infty B_\nu(T) d\nu}, \tag{27}$$

$$k_R^{-1}(P, T) = \frac{\int_0^\infty k_\nu^{-1}(P, T) dB_\nu(T)/dT \, d\nu}{\int_0^\infty dB_\nu(T)/dT \, d\nu}. \tag{28}$$

The Planck mean is weighted toward spectral regions with large opacities; yields the correct flux emitted by an atmospheric layer of temperature T; and is best applied in the higher, more optically thin regions of an atmosphere. Conversely, the Rosseland mean is weighted toward spectral regions of low opacity and ensures the radiation diffusion limit in the opaque regions of an atmosphere (Mihalas 1970, p. 38).

Tabulating Planck and Rosseland mean opacities as a function of temperature and pressure using precomputed, high-resolution gas opacities is a difficult and tedious task. This is especially true for the Rosseland mean, whose weighting toward low-opacity spectral regions places extra emphasis on the poorly understood far wings of spectral lines. Earlier models relied on Tsuji (1971) for gray opacities. More recently, Freedman et al. (2008, 2014) presented tables of Rosseland and Planck mean opacities appropriate for use in brown dwarf and gas giant thermal structure models.

6.4.2. Band models. At the scale of molecular bands, numerous so-called band models have been historically applied to determine thermal radiative fluxes in planetary and stellar atmospheres. Although not widely used today, band models take advantage of the overall smooth nature of band-averaged transmission functions (particularly true for the relatively dense and cool brown dwarf and giant planet atmospheres), $\mathcal{T}_{\Delta\nu}$, with

$$\mathcal{T}_{\Delta\nu} = \frac{1}{\Delta\nu} \int_{\Delta\nu} \mathcal{T}_\nu d\nu = \frac{1}{\Delta\nu} \int_{\Delta\nu} e^{-[\tau_\nu(P_2) - \tau_\nu(P_1)]} d\nu, \tag{29}$$

where P_1 and P_2 are atmospheric pressures (with $P_2 > P_1$), and the final step uses the definition of transmissivity. The band-average transmission functions for an individual gas can be tabulated using high-resolution, wavelength-dependent opacities and are often parameterized by a fit to a particular type of band model, such as the Godson, Malkmus, or Elsasser models (Goody & Yung 1989, their chapter 4). The treatment of band-averaged transmission functions is more complicated in spectral regions where more than one absorbing gas have overlapping features (see Pierrehumbert 2010, his section 4.4.5), but, nevertheless, combined transmission functions can be used to solve the two-stream thermal RTE.

A particular type of band model, the just overlapping line approximation (JOLA), was used in early studies of brown dwarf atmospheres by Allard and collaborators (e.g., Allard & Hauschildt 1995) and by Tsuji and collaborators (Tsuji 1984, 1994, 2002). Carbon (1979) reviews this and other types of band models.

6.4.3. Correlated-k. Spectral integrals of functions that have complicated variation in wavelength (e.g., Equation 29) are computationally expensive. However, over a wavelength range where the source function and the scattering properties of the atmosphere can be taken to be roughly constant, a great deal of computational efficiency can be gained by using the distribution of opacities to replace the integral over frequency with a more well-behaved integral over a new dependent variable. This, effectively, reorders the opacities in wavelength space, creating a smooth, monotonic description of the absorption coefficients and is the root of the k-distribution approach (Ambartzumian 1936, Kondratyev 1965, Arking & Grossman 1972, Domoto 1974).

Given the distribution function of gas opacities, $f(k)$ [where then the fraction of absorption coefficients between k and $k + dk$ is $f(k)dk$], the mean transmission through an atmospheric layer (Equation 29) can be expressed as (see Goody & Yung 1989, their section 4.8)

$$\mathcal{T}_{\Delta\nu} = \int_0^\infty f(k)e^{-k\mathcal{M}}dk, \qquad (30)$$

where the distribution function is over the interval $\Delta\nu$, and $\mathcal{M}$ is the column mass of the layer. Because the distribution function is a relatively smooth function of k, the integral in Equation 30 can be computed with much less computational effort than that in Equation 29. The integral in Equation 30 can be made more straightforward if we replace the distribution function with the cumulative distribution function, $g(k)$, with

$$g(k) = \int_0^k f(k')dk', \qquad (31)$$

so that the mean transmission is then

$$\mathcal{T}_{\Delta\nu} = \int_0^1 e^{-k_g\mathcal{M}}dg, \qquad (32)$$

where k_g indicates the mapping between k and g (i.e., k_g is the value of k that corresponds to the independent variable g). Given the smooth, monotonic nature of $g(k)$, this integral can be accurately evaluated using only ~ 10 intervals in g or less (Goody et al. 1989).

Instead of determining the transmission over $\Delta\nu$ using Equation 32 and then solving the RTE, which would not allow for the treatment of scattering, many k-distribution models use the k–g mapping to determine characteristic absorption coefficients for ranges of g instead (Yamamoto et al. 1970, Lacis & Hansen 1974, Liou 1974, Ackerman et al. 1976, Mlawer et al. 1997), called k coefficients. Along with the relevant thermal and scattering source terms (assumed constant over $\Delta\nu$), the k coefficients are then used to solve the RTE. The fluxes from these calculations are then combined on the basis of the width of the range of g-values used, effectively swapping the order of integration over frequency with the solving of the RTE. As opacities depend on temperature, pressure, and gas composition, the k coefficients must be computed for each model atmospheric layer or, most commonly, obtained from pretabulated results.

In practice, two key complications arise when using k distributions to perform radiative transfer calculations in inhomogeneous atmospheres. First, the particular ordering of opacities in wavelength space that maps to $g(k)$ for a particular atmospheric level need not be the same ordering as at any other level in the model. If the absorption coefficients are indeed spectrally uncorrelated with those at another level, then different wavelengths are being mixed when solving the RTE for the entire atmosphere. Thus, it is assumed, as is often the case, that absorption coefficients throughout the atmosphere are spectrally correlated, leading to the so-called correlated-k method (Lacis & Oinas 1991). In practice this limitation can be overcome by using narrow spectral intervals and choosing interval boundaries so that one main absorber dominates each interval.

Second, the blending of k coefficients, computed for an individual gaseous species, with those for other species to represent a realistic mixture of gases in an atmosphere remains controversial. Most correctly, the k coefficients should be computed for a mixture of gases, but it is often the case in atmospheric modeling that gas mixing ratios are not known a priori (which happens when, e.g., the concentration of a gas depends on other atmospheric state variables). Thus, a more flexible approach is to compute the k coefficients for each individual gas, and then blend these "on the fly" in model runs. However, as discussed by Goody et al. (1989), this approach is only valid when the absorption coefficients for the individual gases are spectrally uncorrelated. Furthermore, blending k coefficients for gas mixtures can be computationally expensive, as the number of permutations

grows exponentially with the number of absorbers. Because of the uncertain magnitude of the error introduced by blending single-gas k coefficients, this approach should only be used with some care.

Complications aside, correlated-k techniques have proven to be efficient and accurate. Extensive testing in the Earth science literature has shown that correlated-k methods can achieve flux and heating rate accuracies to within 1–5%, when compared with more precise techniques (Lacis & Oinas 1991, Fu & Liou 1992, Mlawer et al. 1997). Goody et al. (1989) note occasional cases in which errors are much larger than several percent and caution that expanding the use of correlated-k techniques into new applications (i.e., beyond the Earth sciences) requires testing against more reliable methods to ensure the validity of the approach. Internal tests by the Marley/Saumon group have found that, for cloud-free models, the correlated-k approach is accurate to within approximately 1% in flux for brown dwarfs when compared with rigorous line-by-line calculations—this is a level of accuracy that exceeds most other uncertainties in the problem.

6.4.4. Line-by-line. At spectral scales in which the radiative source terms and all opacity sources can be considered to be constant (i.e., at resolutions typically less than approximately 0.01 cm^{-1}), radiative transfer calculations are monochromatic and computing spectrally averaged opacities is no longer an issue. Models that solve the monochromatic RTE over a fine grid of wavelengths are referred to as line-by-line radiative transfer models. This technique is considered to be the most accurate method for dealing with complex opacities, but the brute force nature of the approach makes the technique computationally expensive. High-resolution methods can be made more efficient using spectral mapping techniques (West et al. 1990, Meadows & Crisp 1996), in which monochromatic elements with similar optical properties at all atmospheric levels are binned together, with the RTE being solved only once for the bin instead of for every monochromatic element.

A sample comparison between a line-by-line model spectrum (T_{eff} = 2,200 K) and data for an L2 dwarf at a spectral resolution of $\lambda/\Delta\lambda$ = 50,000 is shown in **Figure 8**. This spectral resolution, which is much higher than typical brown dwarf spectra, is sufficient to resolve individual lines. Although the model (from Marley et al. 2002) has been convolved with a rotational kernel, the overall agreement in this particular case demonstrates that the model line broadening treatment generally reproduces the data. Note that this particular model employed assumes no microturbulent broadening.

Finally, direct opacity sampling (dOS) (Hauschildt et al. 2001), like line-by-line calculations, solves the RTE monochromatically and is the method for handling opacities in the RTE currently used in the PHOENIX group of models (Allard & Hauschildt 1995, Barman et al. 2001). Note that dOS is distinguished from standard opacity sampling methods, which use statistical techniques (e.g., weighting by a Planck function) to sample the wavelength-dependent opacity distribution in that dOS uses a prespecified spectral grid, which can be set to very fine resolutions. In practice, computational cost limits dOS calculations to ∼1 cm^{-1}, which is sufficient to accurately compute the radiative fluxes but is not as fine as true line-by-line calculations.

7. CLOUD OPACITY

The problem of modeling clouds in ultracool dwarfs and giant planets is a central challenge to understanding the atmospheric structure, reflected and emitted spectra, and evolution of these objects. The subject is complex, and there are many different approaches. In this section, we give an overview of the problem and some perspective on the various modeling approaches. A more detailed review is given by Marley et al. (2013), and detailed comparisons of cloud treatments have been given by Helling et al. (2008a) (which is now slightly dated).
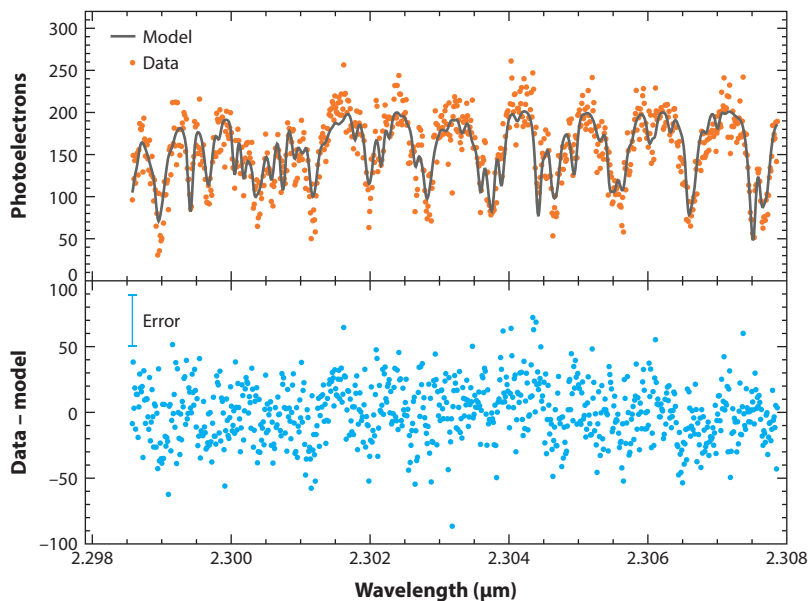
Figure 8

Comparison of a model spectrum to observations of the L2 dwarf 2MASS J01090150-5100494 (from Blake et al. 2007), obtained at a spectral resolution of approximately $\lambda/\Delta\lambda = 50,000$. The top panel shows the observed data as small points (*orange*) with a best-fit model overplotted as a line (*gray*, with $T_{\text{eff}} = 2,200$ K and $g = 10^3$ m s^{-2}). The bottom panel shows the residuals of this fit (*blue*), and the error bar in the upper left corner approximates the expected noise (photon and read noise) of the spectrum. The agreement indicates that, in this case, the model line shapes (primarily due to H_2O and CO lines) do a good, although not perfect, job of reproducing the observations even at this high resolution.

7.1. Condensates Overview

As in the cool, dense molecular atmospheres found within the Solar System, a variety of species condense within the atmospheres of brown dwarfs. The resulting clouds present the single greatest obstacle impeding our understanding of these objects. To correctly account for cloud opacity, it is necessary to model each condensate-forming species, estimating particle sizes and vertical distributions. Predicting whether condensates are submicron in size and are distributed vertically throughout the atmosphere, to millibar pressures for example, or whether particles are large and mostly confined to thin cloud decks, or are something in between is the central task of condensate modeling. The difficulty in accomplishing this, and of reconciling diverse modeling approaches with data, limits progress and understanding. Although a number of innovative and insightful cloud models have been developed to facilitate modeling of brown dwarf atmospheres and the interpretation of data, there has been remarkably little progress in the past decade, and the problem of cloud opacity provides the greatest opportunity to realize improvements in model atmosphere fidelity.

At the relatively cool atmospheric temperatures of brown dwarfs and giant planets, important atmospheric constituents are expected to be found in condensed phases, particularly Fe, Si, and Mg, but also the more refractory components, including Al, Ca, Ti, and V. **Table 1** lists many of the important condensates predicted by rainout chemical equilibrium.

For the case of homogeneous condensation, in which the gas phase species condenses to form a solid or liquid of the same species (e.g., Fe or H_2O), condensation first occurs in a rising parcel of gas when the local partial pressure of the condensing gas first exceeds the saturation vapor

Table 1 Selected elemental abundances and species of interest

Element	Relative abundance[a] $\log[n(El)/n(H)] + 12$	Important species[b] (rainout chemistry)
H	12	H_2, H
He	10.9	He
O	8.7	CO, H_2O (v, s, l), silicates
C	8.4	CO, CH_4, CO_2
N	7.8	N_2, NH_3 (v, s), NH_4SH (s)
Mg	7.6	$MgSiO_3$ (s), Mg_2SiO_4 (s), MgH
Fe	7.5	FeH, Fe (l, s)
S	7.2	H_2S, NH_4SH (s), MnS (s), Na_2S (s), ZnS (s)
Al	6.5	Al_2O_3 (s),
Na	6.3	Na, Na_2S (s)
P	5.5	PH_3, P_4O_6
K	5.1	K, KCl (s)
Ti	4.9	TiO, $CaTiO_3$ (s)
V	4.0	VO, V-oxides

[a]Abundances from Lodders (2003).
[b]See Lodders (2010) for a review.
Abbreviations: l, liquid; s, solid; v, vapor.

pressure. This defines the cloud base. Supersaturation is a measure of how far in excess of the saturation vapor pressure the gas must be in order to condense. In more complex cases (e.g., Ca and TiO forming $CaTiO_3$) the cloud base is determined in principle through chemical equilibrium calculations. **Figure 9** shows the condensation boundaries, again for rainout chemistry, for many key species along with a collection of model pressure-temperature profiles for reference. The marked boundaries in the figure are the locations where the labeled solid or liquid species form as its progenitor gaseous species are carried upward in a rising air parcel.

As **Figure 9** attests, there are numerous atmospheric condensates within the brown dwarf pressure-temperature regime. However, not all of them are equally important. Some species, such as TiO, play a leading role in controlling gaseous opacity in the M and early L dwarfs but, because of their low abundance, are relatively unimportant cloud opacity sources. The more abundant Fe-, Si-, and Mg-bearing species have a greater contribution to column grain optical depths. The role of elemental abundances and particle sizes can best be appreciated by constructing a highly simplistic cloud model (Marley 2000), a task that also illustrates the challenge faced by cloud modelers.

If we assume that all molecules of a species with a fractional number mixing ratio, f, resident above a given pressure level, P_c, condense, then, for a hydrostatic atmosphere, the column mass of the condensate, $\mathcal{M}_c$, is given by

$$\mathcal{M}_c = f\left(\frac{m_c}{m}\right)\left(\frac{P_c}{g}\right), \tag{33}$$

where m_c is the molecular mass of the condensed species, and m is the mean molecular mass of the atmosphere. **Table 2** gives $\varphi = fm_c/m$ and the condensation temperature at 3 bar in a solar composition gas for several important species. Given this column mass, the total condensate optical depth as a function of wavelength, λ, can be estimated given the particle size, r_c, the extinction
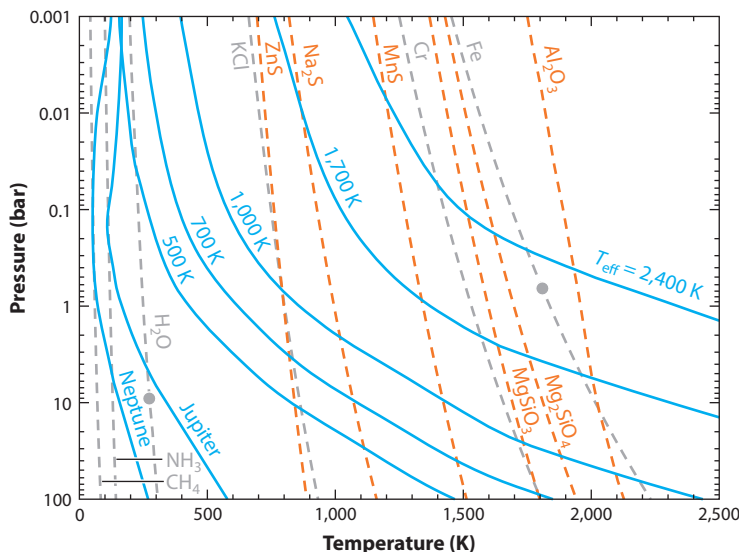
Figure 9

Condensation curves for a variety of species (*dashed*), assuming solar abundances from Lodders (2003). Gray curves are for direct condensation, whereas orange curves are for condensates that form as a result of chemical reactions. Filled circles indicate a liquid-solid transition. Several cloud-free model thermal profiles are provided for comparison, as well as empirically derived profiles for Jupiter and Neptune.

efficiency, $Q_\lambda^{\text{ext}}(r_c)$ (which can be derived from Mie theory), and the condensate mass density, ρ_c,

$$\tau_\lambda = 75\epsilon \, Q_\lambda^{\text{ext}}(r_c)\varphi \left(\frac{P_c}{1\,\text{bar}} \right) \left(\frac{10^5\,\text{cm s}^{-2}}{g} \right) \left(\frac{1\,\mu\text{m}}{r_c} \right) \left(\frac{1\,\text{g cm}^{-3}}{\rho_c} \right). \qquad (34)$$

In a real atmosphere, not all the condensable species are found in the condensed phase, so this parameterization introduces a term, $\epsilon < 1$, to account for such effects.

Equation 34 exemplifies many of the challenges presented by atmospheric condensates. Although we can estimate the column mass of a given material that may be found in the condensed phase, the actual opacity depends sensitively upon the particle size through both the mass partition term and the Mie extinction. **Figure 10** shows spectra of Mie absorption and scattering efficiencies, in which $Q_\lambda^{\text{ext}} = Q_\lambda^{\text{abs}} + Q_\lambda^{\text{scat}}$, for a collection of condensates and for several different particle sizes. Furthermore, the mass balance in Equation 34 tells us nothing about the vertical

Table 2 Parameters for elementary cloud model of selected condensates

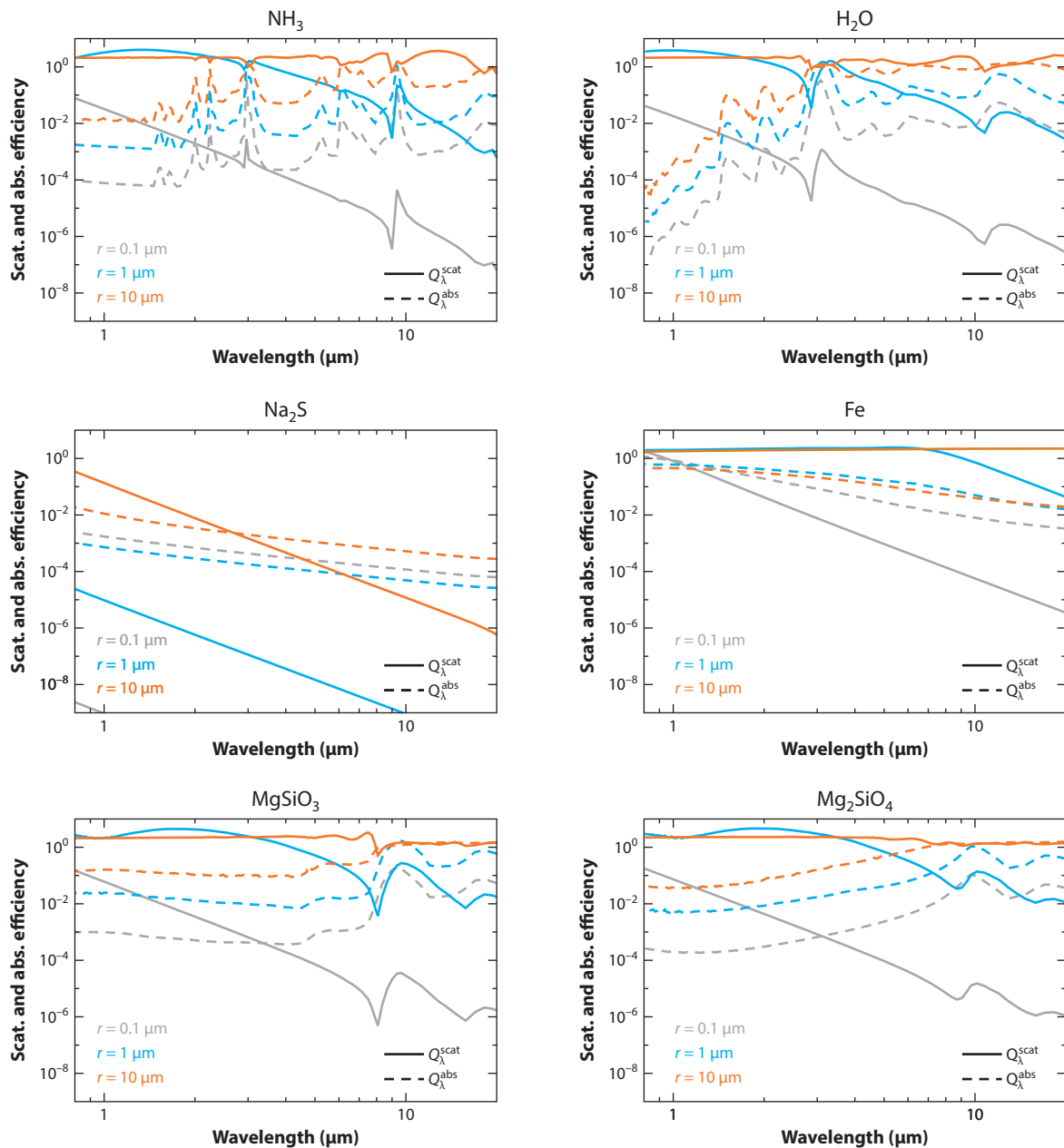| Species	f	$\varphi = f\frac{m_c}{m}$	T_{cond} at 3 bar (K)
H_2O	1.2×10^{-3}	9.7	265
KCl	2.2×10^{-7}	7.1×10^{-3}	820
Na_2S	1.7×10^{-6}	5.8×10^{-2}	1,025
$MgSiO_3$	5.9×10^{-5}	2.6	1,685
Mg_2SiO_4	3.0×10^{-5}	1.8	1,760
Fe	5.3×10^{-5}	1.3	1,930
$CaTiO_3$	1.4×10^{-7}	8.4×10^{-3}	2,010

Figure 10

Absorption and scattering efficiencies for six different condensable species computed using Mie theory. In each panel, the Mie scattering and absorption efficiencies, Q_λ^{scat} (*solid*) and Q_λ^{abs} (*dashed*), respectively, are shown for three particle sizes—0.1 μm (*gray*), 1 μm (*blue*), and 10 μm (*orange*). Larger particles are more efficient at both absorbing and scattering for most wavelengths. Figure adapted from Morley et al. (2014b) with permission.

distribution of the grains above a condensation level. An additional limitation, of course, is that basic Mie theory (for a modern review of the history of the method and summary of available codes, see Wriedt 2012) assumes that the condensates are ideal, spherical particles.

All else being equal, however, reference to **Table 2** demonstrates that knowing the fractional abundance of a condensate is crucial to understanding its potential contribution to cloud opacity. The single most important condensate over the range of temperatures expected for brown dwarf atmospheres is H_2O. Iron and silicate phases are the second most important species, whereas the refractory oxides, such as $CaTiO_3$, and the alkali species, such as KCl, are of tertiary importance.

7.2. Modeling Approaches

One could begin to compute the vertical distribution of cloud opacity by considering several possible fates for atmospheric grains after they have formed. In one extreme, the grains may immediately fall out of the atmosphere, leaving behind a clean gas. Fortuitously, the first indisputable brown dwarf, Gliese 229B, could be well described by such an atmosphere, and models that entirely neglected grain opacity did a reasonable job of reproducing the observed spectra. Many groups today continue to produce cloud-free models, although they differ in the details of how the chemistry is treated. Examples include the COND models of the PHOENIX group and various model formulations from other groups, including the cloudless models of Saumon & Marley (2008). At the other extreme, grains may stay in chemical equilibrium with the local gas and not precipitate at all. This is the domain of the DUSTY models of Allard et al. (2001). Recall that these two extremes also describe treatments of rainout chemistry discussed in Section 5.1.2. All other cloud models attempt to define some intermediate case in which grains grow and fall from the upper reaches of the atmosphere but do not completely disperse, thus forming cloud decks of some finite vertical extent.

One approach attempts to empirically describe clouds by varying only a few parameters. Typically this is a cloud bottom, at the condensation level, and top pressure (or, equivalently, a bottom pressure and fractional vertical scale height) and a particle size. Examples of such defined cloud models include the unified models of Tsuji et al. (Tsuji 2002) and various cloud models employed by Burrows and collaborators (Burrows et al. 2002, Currie et al. 2011). The strength of this approach is that no cloud physics need be crafted but rather a set of empirical cloud descriptions can be accumulated as progressively more objects are compared with models. In principle, more sophisticated models could be constructed that attempt to explain trends in particle sizes or cloud thicknesses once a sufficient number of objects have been characterized. In practice, however, this has not yet happened, and we are left with individualized descriptions of particular objects. This approach also has little predictive value, as it is not obvious what parameters may be appropriate to describe new objects.

Nevertheless, the defined cloud method has contributed to the definitive finding that neither the cloudless nor fully dusty concepts are correct for the L dwarfs—brown dwarf clouds are found in discrete layers, as are clouds throughout the Solar System. Indeed, this limitation of the DUSTY modeling approach is an important one. Because the DUSTY models assume that condensates do not form cloud layers, for cooler models the atmospheric column becomes optically thick very rapidly, even when just accounting for the grain opacity. By $T_{eff} \sim 1,300$ K, DUSTY models are far redder, with far shallower molecular bands, than even the cloudiest known L dwarfs. For this reason, fits of DUSTY models to data seldom find effective temperatures below 1,400 K or even 1,500 K.

One example of a model that attempts to capture some aspects of cloud physics to predict particle sizes and vertical distributions is the `Eddysed` model developed by Ackerman & Marley

(2001). This model balances upward and downward transport of condensable gases and condensates by way of a tunable sedimentation efficiency parameter, f_{sed}. As f_{sed} increases, downward mass transport by falling particles becomes more efficient, and the clouds become thinner. The code computes the particle sizes that are required to produce the implied mass balance rather than attempting to model grain growth explicitly. A more comprehensive discussion of this model framework and its applications to giant planet and brown dwarf atmospheres is given by Marley et al. (2013, their section 4.5).

A unique cloud modeling paradigm has been developed by Helling et al. in a series of papers (e.g., Helling et al. 2001, 2008a,c; Helling & Woitke 2006, and references therein). The key underlying assumption of this approach is that—not unlike the conversion of CO to CH_4—condensation is difficult; the formation of many of the condensates predicted by chemical equilibrium requires the collisions and reactions of multiple gaseous components (e.g., Ca and TiO molecules, both of which are relatively rare in the predominantly H_2-He gas). This approach thus posits that an equilibrium progression of distinct cloud layers, as predicted by equilibrium chemistry, is unlikely. Instead this paradigm follows the growth of condensate seed particles that fall down from the top of the atmosphere, facilitating the nucleation of a sequence of compounds that are formed during the downward drift of particles from above. Instead of the canonical equilibrium cloud layers, this approach predicts a blend of dirty grains, with a complex, mixed composition that varies continuously with height.

Helling and collaborators have explored the various ramifications of this approach in greater detail than can be summarized here (recently by Witte et al. 2011). The main takeaway is that the canonical condensation sequence of **Figure 9** is an overly idealized conception of reality. However, to reach this conclusion, the Helling et al. model posits what may be an equally unlikely scenario: The highly refractory seed particles are taken to be carried by strong updrafts from the deep atmosphere to the top of the atmosphere, where they begin their downward journey. These TiO_2 particles are presumed to be transported upward rapidly enough such that no condensation takes place onto these nuclei and that none of the other condensable species that are also entrained in the updraft condense during the upward journey. In the limit of cold Solar System giant planets, we know that this is not the case as there is no such high altitude refractory haze observed. Another practical difficulty with this model is that the rich brew of condensates imprints a complex signature on models of emergent spectra such that it is challenging to appreciate the effect of any single component of the model.

Despite the aforementioned concerns, there is much to recommend the Helling et al. viewpoint, and only detailed comparisons of model predictions to data will ascertain the validity of this model conception. Indeed the Drift-PHOENIX set of forward models has adapted a version of the Helling et al. models, although as of the time of preparation of this review, the models have not been described in the literature.

8. DERIVING THE THERMAL PROFILE

In practice, a one-dimensional radiative-convective thermal structure profile must be derived iteratively, starting from a first guess. There are several approaches that can be followed to determine the equilibrium profile, which satisfies Equation 4, and where the temperature and flux profiles are all continuous. A straightforward technique is to simply timestep the atmosphere to equilibrium, which dates back to some of the earliest radiative-convective models (Manabe & Strickler 1964). However, more efficient computational approaches to determining the equilibrium thermal structure have been developed and, here, simply as a means of bringing together the previous sections, we sketch out one technique that has been successfully applied to Solar System, extrasolar planet,

and brown dwarf atmospheres (McKay et al. 1989, Marley et al. 1996, Marley & McKay 1999, Fortney et al. 2005).

We begin with an atmosphere grid that has some number, N, of discrete levels, denoted by i (**Figure 1**). The topmost level is taken as $i = 1$, and each level is associated with a fixed pressure. If the radiative-convective boundary falls at level i_{RC}, then, as was discussed in Section 4.1, the temperature at each point in the convection zone (i.e., the points for which $N \geq i \geq i_{RC}$) can be found by following an adiabatic gradient downward from the temperature at the radiative-convective boundary, T_{RC}. Thus, our task is to solve for the temperature at each level for which $i \leq i_{RC}$. Here, the atmosphere is in radiative equilibrium and, for nonirradiated bodies, the net thermal flux through each level must be (from Equation 4)

$$F_{i,\text{target}}^{\text{net}} = \sigma T_{\text{eff}}^4, \tag{35}$$

where T_{eff} is the desired effective temperature for the model, and the thermal subscript has been dropped for clarity. For irradiated planets, the net thermal flux must be increased by the net stellar flux at each level.

For a first guess atmosphere profile $T(P)$, chemical abundances must be determined (Section 5) and distributions of any relevant aerosols must be found (Section 7). From these, the wavelength-dependent opacities can be computed (or obtained from a look-up table; Section 6), thereby permitting the calculation of the net thermal flux profile (Section 3). In general, though, the net thermal fluxes at the model levels throughout the radiative zone will not sum to the target value, implying a net radiative heating or cooling (Equation 5). From the mismatch with the target, a flux error can be computed and is given by $\delta F_i^{\text{net}} = F_i^{\text{net}} - F_{i,\text{target}}^{\text{net}}$. The task of the model is then to correct the first guess $T(P)$ profile to find an improved guess. This is a complex problem, as the flux at each level in the atmosphere depends on the temperature structure of all other layers. So $F_i^{\text{net}} = F_i^{\text{net}}(T_1, T_2, T_3, \ldots, T_{RC})$. Note that, because T_{RC} controls the temperature profile down the adiabatic gradient through the convection zone, F_i^{net} does not explicitly depend on the temperature at levels with $i > i_{RC}$, as these temperatures are uniquely specified by T_{RC} and the adiabat.

A Jacobian matrix, $\overset{\leftrightarrow}{\mathbf{A}}$, of partial derivatives describes how the flux at each level in the atmosphere depends upon the temperature at each level,

$$\overset{\leftrightarrow}{\mathbf{A}} = \begin{pmatrix} \dfrac{\partial F_1}{\partial T_1} & \dfrac{\partial F_1}{\partial T_2} & \cdots & \dfrac{\partial F_1}{\partial T_{RC}} \\ \dfrac{\partial F_2}{\partial T_1} & \dfrac{\partial F_2}{\partial T_2} & \cdots & \dfrac{\partial F_2}{\partial T_{RC}} \\ \vdots & \vdots & \ddots & \vdots \\ \dfrac{\partial F_{RC}}{\partial T_1} & \dfrac{\partial F_{RC}}{\partial T_2} & \cdots & \dfrac{\partial F_{RC}}{\partial T_{RC}} \end{pmatrix}. \tag{36}$$

The individual terms in the Jacobian matrix are computed by iteratively perturbing the temperature at each level in the model and recomputing the net fluxes throughout the atmosphere. This is a time-consuming step as the entire radiative transfer must be solved i_{RC} times, each occasion with a temperature perturbation introduced at a single level. Once $\overset{\leftrightarrow}{\mathbf{A}}$ is in hand it must be inverted to find the vector,

$$\delta \mathbf{T} = \overset{\leftrightarrow}{\mathbf{A}}^{-1} \cdot \delta \mathbf{F}, \tag{37}$$

where $\delta \mathbf{F}$ is the vector of flux errors. Then $\mathbf{T}_i' = \mathbf{T}_i + \delta \mathbf{T}_i$ would ideally bring all the net thermal fluxes to the desired value (i.e., Equation 35).

Once a temperature correction is applied and a new thermal structure is in hand, the process repeats. In practice, the new model will not be precisely at $\mathbf{F}_{\text{target}}^{\text{net}}$ because the problem is not

linear, and molecular abundances, opacities, and cloud structures should all respond to the new profile, further perturbing the computed fluxes. Thus, many iterations are required until the net fractional thermal flux change from one iteration to the next is smaller than some small target value throughout the atmosphere, typically taken as 10^{-5}–10^{-6}. In addition, if the temperature gradient in the bottom-most radiative layer exceeds the adiabatic lapse rate, then the lapse rate in that layer must be reset to the adiabatic value and the radiative-convective boundary moved up to level $i_{RC} - 1$. In practice there are many more subtleties that arise, but, nevertheless, approaches such as this are robust and eventually converge on a desired solution.

The computational intensity of the process outlined above, particularly the repeated calculation of $\vec{\vec{A}}$ and the attendant radiative transfer calculations, is the reason why rapid methods for computing the radiative transfer are required for atmospheric modeling (e.g., Section 6.4). Additionally, various methods for streamlining this process and minimizing the number of matrix inversions that must be performed have been devised.

The greatest impediment to model convergence is, of course, clouds. If an iterative step cools the overall profile, then the cloud base for a photospheric condensate moves down to thicker atmospheric levels and, as a result, the cloud optical depth increases. However, a thicker cloud traps more thermal radiation in the atmosphere (i.e., provides a stronger greenhouse effect), which, in turn, tends to heat the atmosphere and warm the temperature profile. This, then, leads to a higher cloud base, a thinner cloud, and greater cooling. Without some numerical approach to smooth convergence, it is not unusual to see model profiles vacillate among different cloud states while never converging to a mean solution. In modern terrestrial cloud modeling, in fact, clouds are never treated in one dimension because of this problem. Approaches that have been tried in brown dwarf atmospheric modeling include using trailing averages of past cloud states to smooth out jumps in the cloud state and using two atmospheric columns, one cloudy and one clear, to allow for horizontal patchiness and reduced sensitivity to opacity changes. Details of such numerical tricks are not always well described in the literature.

9. RESULTS

Several research groups actively construct radiative-convective equilibrium atmosphere models, compute emergent spectra, and compare the results to data. **Table 3** lists a few of the most active collaborations and selected theory and model-data comparison papers. These papers serve as jumping-off points to further explore the approaches employed by and the science results of each group.

Figure 11 presents some example comparisons between models computed by the Marley/Saumon group and spectral data for a broad range of L and T dwarfs. Details of the models and data are presented by Stephens et al. (2009). The individual best-fitting models were selected from a large grid of forward models computed for this purpose. As the figure attests, the quality of the matches varies from object to object. Overall the fits for the T dwarfs are generally quite good. Notably for the early (T0 to T2) and the one T5.5 dwarfs, thin clouds ($f_{sed} \sim 3$ to 4) are favored, whereas for the T4 dwarfs cloudless models fit best.

In contrast, for the L dwarfs, generally thicker clouds (f_{sed} mostly in the range of 1 to 2) are required. Cloudless models (not shown) fit far more poorly, thus demonstrating that even though there are no "smoking-gun" spectral features indicating that clouds are present, their overall impact on the spectra are undeniable (the absence of TiO and other spectral features in the spectra of L dwarfs that are found in M dwarfs indicates that these species have condensed but not necessarily into discrete cloud decks). **Figure 11** also demonstrates that although the cloudy models generally reproduce the spectral shapes of each object, there are important mismatches between models and

Table 3 Ultracool modeling schools

School	Key characteristics (chemistry; cloud; opacity)	Selected papers
Barman	True chem. eq.; defined clouds; sampling	Barman et al. 2011
Burrows	True chem. eq.; defined cloud; sampling	Burrows et al. 2002, Currie et al. 2011
Marley/Saumon	Rainout eq.; eddysed[a]; correlated-k	Saumon & Marley 2008, Stephens et al. 2009
PHOENIX	True chem. eq.; various clouds[b]; sampling	Witte et al. 2011
Tokyo	True chem. eq.; UCM[c]; band model	Sorahana & Yamamura 2012, Tsuji 2005

[a]Eddy-sedimentation, a cloud physics model (Ackerman & Marley 2001).
[b]Various cloud physics models, including DUSTY (Allard et al. 2001) and DRIFT (Witte et al. 2011).
[c]The Unified Cloud Model, a defined cloud model (Tsuji 2002).

data. Because we know from the comparisons with the cloudless T dwarfs that the atmospheric chemistry is reasonably well understood, these mismatches point to shortcomings in the cloud model. Understanding the sources of these mismatches and how the cloud description should be modified in each case represents an important task for future research.

Witte et al. (2011) fit many of the same dwarfs as Stephens et al. (2009), and this provides an opportunity to compare derived parameters from two groups. For 2MASS J1507, an L5.5
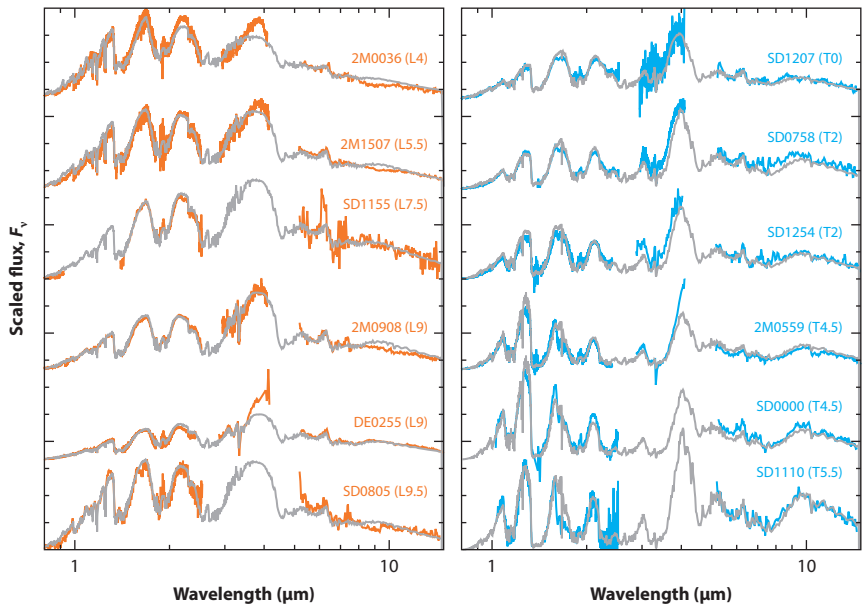
Figure 11

Spectral comparison between observations and best-fit models (*gray*). The left subplot shows L dwarfs (*orange*), and the right shows T dwarfs (*blue*). Spectral types are indicated in parentheses. Adapted from Stephens et al. (2009) with permission, and details regarding data and model properties can be found there.

dwarf, for example, the best fitting model of Stephens et al. (2009) has $g = 3 \times 10^3$ m s^{-2} and $T_{eff} = 1,600$ K. Witte et al., using the cloud model approach of Helling's group (but fitting only to the 1.0- to 3.0-μm data), find $g = 1 \times 10^3$ m s^{-2} and $T_{eff} = 1,800$ K. This discrepancy is almost certainly attributable to the differing cloud models and again points to the need for higher fidelity models or a new approach.

10. CURRENT ISSUES

10.1. Variability and Patchy Clouds

The emergent spectra of many L and T dwarfs are known to vary with time (e.g., Bailer-Jones & Mundt 1999, Tinney & Tolley 1999, Gelino et al. 2002, Artigau et al. 2009, Heinze et al. 2013). Broadband observations have revealed periodic and nonperiodic flux variations as large as 10–30% (Radigan et al. 2012, Gillon et al. 2013), occurring on timescales from 1 to 100 h (Bailer-Jones & Mundt 2001), and spectroscopic observations have shown that variability can be strongly wavelength-dependent (Buenzli et al. 2012). Although a variety of dynamical processes can influence brown dwarf spectra (Robinson & Marley 2014, Zhang & Showman 2014), it is generally expected that clouds play an important, if not central, role in these brightness variations, as cloud structures provide a continuum opacity source that sculpts the emergent spectra of nearly all spectral classes of brown dwarfs. Indeed, a variety of patchy cloud models have demonstrated that, in many cases, observed variability can be explained by changes in cloud distribution and thickness (Marley et al. 2010, Apai et al. 2013, Burgasser et al. 2014, Morley et al. 2014a). Furthermore, a recent report of a spatially resolved map of a nearby L–T transition dwarf (Crossfield et al. 2014) revealed a patchy photosphere consistent with complex cloud structures.

Clearly observations of brown dwarf variability present an important opportunity for constraining cloud models and dynamical simulations. For example, Zhang & Showman (2014) used a simple, cloud-free dynamical model to study how different circulation regimes in brown dwarf atmospheres could influence broadband light curves. However, realistically simulating the influence of patchy, time-evolving clouds on the emergent spectra of brown dwarfs presents a great modeling challenge. The study of brown dwarf atmospheric circulation is only just beginning (e.g., Showman & Kaspi 2013) and, as a result, these models have not yet incorporated chemistry, aerosols, or wavelength-dependent radiative transfer. Meanwhile, one-dimensional brown dwarf atmospheric models, which do incorporate chemistry, clouds, and realistic radiative transfer, are typically only used to study an atmosphere in its steady state. A combination of these two approaches is needed if we are to understand the true nature and complexity of brown dwarf atmospheres.

10.2. Atmospheric Retrieval

The actual atmospheric state of a world, including the thermal structure and gas concentrations, can be constrained by a group of techniques called retrieval. Atmospheric retrieval techniques, somtimes referred to as inverse methods, have their origins in the Earth remote sensing literature (Rodgers 1976, 2000) and operate by extracting information about atmospheric conditions from emitted-, reflected-, or transmitted-light spectra. From the perspective of radiative-convective modeling, the utility of retrieval is obvious—these techniques provide a direct and independent means of constraining the parameters and physics of atmospheric thermal structure models.

Hot Jupiters have seen extensive applications of retrieval techniques. Madhusudhan & Seager (2009), by comparing observations of HD 189733b and HD 209458b to a multidimensional grid of models, reported constraints on the atmospheric thermal structure and concentrations of several key gases for these worlds. More sophisticated retrieval methods have also been applied to
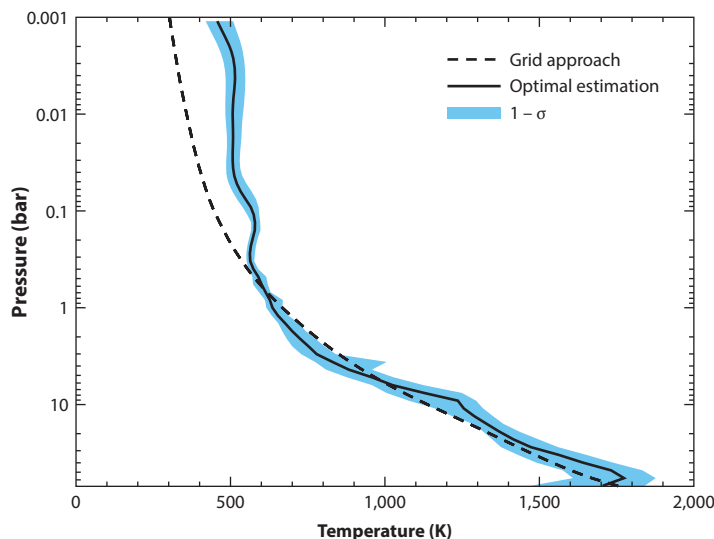
Figure 12

Comparison of two approaches for determining the thermal structure of a brown dwarf, as applied to GL 570D (Burgasser et al. 2000). A grid comparison approach from Saumon et al. (2006) is shown (*dashed*), and a retrieved *P-T* profile (*solid*) with 1-σ error bars (*blue shading*), determined using optimal estimation techniques, is also shown. Figure adapted from Line et al. (2014) with permission.

observations of hot Jupiters, including optimal estimation techniques (Lee et al. 2012, Line et al. 2012) and Markov chain Monte Carlo methods (Madhusudhan et al. 2011, Benneke & Seager 2012, Line et al. 2013). Care must be taken when interpreting retrieval results, especially when constrained only by photometric data, as the results hinge on the assumptions incorporated into the forward model, including the particular set of gases included.

Historically, evolutionary and atmospheric processes of brown dwarfs have been constrained by comparing observed spectra of individual objects to a large grid of model spectra (e.g., Burrows et al. 1993, Burgasser et al. 2007). Uncertainties in key parameters (e.g., effective temperature) are sometimes estimated within the grid-based model comparison approach (Cushing et al. 2008, Rice et al. 2010). A drawback of this approach is that it imposes model assumptions onto the resulting fits, and the fitting approach amounts to hunting for the model parameters that best reproduce an observed spectrum.

Very recently, optimal estimation retrieval techniques have been applied to hot, young, directly imaged gas giant planets (Lee et al. 2013) and brown dwarfs (Line et al. 2014). **Figure 12** compares thermal profiles from a grid-based approach (Saumon et al. 2006) and an optimal estimation retrieval approach (Line et al. 2014), as applied to GL 570D (Burgasser et al. 2000). The agreement between the two methods is quite good, except in the upper atmosphere, where the optimal estimation approach indicates a warmer thermal structure. This result hints that important physics may be missing from the models used in the grid-based approach, such as nonlocal thermodynamic equilibrium processes (Sorahana et al. 2014).

11. CONCLUSION

Since the discovery of the first unmistakable brown dwarf in 1995 there have been well over 3,000 papers published on this topic alone. Almost without exception, these papers, which generally aim

to understand the spectra, formation, and evolution of brown dwarfs, relate in one way or another to the atmospheres of these objects. Although the numbers of papers about the directly imaged planets are—for now—smaller, there is little doubt that this field is likewise on the verge of a rapid expansion.

The science yield from new exoplanet discoveries, as well as from ongoing studies of brown dwarfs, hinges in large part on our ability to model and understand the atmospheres of these worlds. Although the first two decades of brown dwarf science has seen remarkable advances in the fidelity of atmosphere modeling, there is still much room for improvement. Better cloud models, greater exploration of the effect of varying elemental abundances, particularly atmospheric C/O ratios, and greater studies of departures from equilibrium chemistry are all important areas for improvement. Ultimately, retrieval methods for determining atmospheric thermal, cloud, and chemical profiles likely offer the best avenue for truly constraining the properties of these objects. Retrieval methods, however, require high-fidelity data—ideally taken over a large wavelength range—and this may be difficult for directly imaged exoplanets in the foreseeable future.

Nevertheless, the convergence of modeling approaches derived from the studies of Earth, Solar System planets, exoplanets, and, of course, stellar atmospheres will continue to enrich this field. Brown dwarfs are often explained as being failed stars, but there is little doubt that the study of their complex, fascinating atmospheres has been one of the great successes of theoretical astrophysics over the past two decades.

DISCLOSURE STATEMENT

ACKNOWLEDGMENTS

LITERATURE CITED

Ackerman AS, Marley MS. 2001. *Ap. J.* 556:872
Ackerman TP, Liou KN, Leovy CB. 1976. *J. Appl. Meteorol.* 15:28
Allard F, Hauschildt PH. 1995. *Ap. J.* 445:433
Allard F, Hauschildt PH, Alexander DR, Starrfield S. 1997. *Annu. Rev. Astron. Astrophys.* 35:137
Allard F, Hauschildt PH, Alexander DR, Tamanai A, Schweitzer A. 2001. *Ap. J.* 556:357
Allard F, Hauschildt PH, Baraffe I, Chabrier G. 1996. *Ap. J. Lett.* 465:L123
Allard NF, Kielkopf JF, Spiegelman F, Tinetti G, Beaulieu JP. 2012. *Astron. Astrophys.* 543:A159
Allende Prieto C, Lambert DL, Asplund M. 2001. *Ap. J. Lett.* 556:L63
Allende Prieto C, Lambert DL, Asplund M. 2002. *Ap. J. Lett.* 573:L137

Ambartzumian V. 1936. *Publ. Obs. Astron. Univ. Leningrad* 6:7

Anders E, Grevesse N. 1989. *Geochem. Cosmochim. Acta* 53:197

Andrews DG. 2010. *An Introduction to Atmospheric Physics*. Cambridge, UK: Cambridge Univ. Press

Apai D, Radigan J, Buenzli E, et al. 2013. *Ap. J.* 768:121

Arking A, Grossman K. 1972. *J. Atmos. Sci.* 29:937

Artigau É, Bouchard S, Doyon R, Lafrenière D. 2009. *Ap. J.* 701:1534

Asplund M, Grevesse N, Sauval AJ, Scott P. 2009. *Annu. Rev. Astron. Astrophys.* 47:481

Bailer-Jones CAL, Mundt R. 1999. *Astron. Astrophys.* 348:800

Bailer-Jones CAL, Mundt R. 2001. *Astron. Astrophys.* 367:218

Baraffe I, Chabrier G, Allard F, Hauschildt PH. 2002. *Astron. Astrophys.* 382:563

Barman TS, Hauschildt PH, Allard F. 2001. *Ap. J.* 556:885

Barman TS, Macintosh B, Konopacky QM, Marois C. 2011. *Ap. J.* 733:65

Barshay SS, Lewis JS. 1978. *Icarus* 33:593

Benneke B, Seager S. 2012. *Ap. J.* 753:100

Beuzit JL, Feldt M, Dohlen K, et al. 2008. In *Ground-based and Airborne Instrumentation for Astronomy II*, ed.
    IS McLean, MM Casali. *Proc. SPIE Conf. Ser.* 7014:701418. Bellingham, WA: SPIE

Bézard B, Lellouch E, Strobel D, Maillard JP, Drossart P. 2002. *Icarus* 159:95

Bishop J, Atreya SK, Romani PN, et al. 1995. In *Neptune and Triton*, ed. DP Cruikshank, MS Matthews, AM
    Schumann, p. 427. Tucson: Univ. Ariz. Press

Blake CH, Charbonneau D, White RJ, Marley MS, Saumon D. 2007. *Ap. J.* 666:1198

Böhm-Vitense E. 1958. *Z. Astrophys.* 46:108

Brown LR, Plymate C. 1996. *J. Quant. Spectrosc. Radiat. Transf.* 56:263

Buenzli E, Apai D, Morley CV, et al. 2012. *Ap. J. Lett.* 760:L31

Bulanin M, Dokuchaev A, Tonkov M, Filippov N. 1984. *J. Quant. Spectrosc. Radiat. Transf.* 31:521

Burgasser AJ, Cruz KL, Kirkpatrick JD. 2007. *Ap. J.* 657:494

Burgasser AJ, Gillon M, Faherty JK, et al. 2014. *Ap. J.* 785:48

Burgasser AJ, Kirkpatrick JD, Cutri RM, et al. 2000. *Ap. J. Lett.* 531:L57

Burrows A, Burgasser AJ, Kirkpatrick JD, et al. 2002. *Ap. J.* 573:394

Burrows A, Hubbard WB, Lunine JI, Liebert J. 2001. *Rev. Mod. Phys.* 73:719

Burrows A, Hubbard WB, Saumon D, Lunine JI. 1993. *Ap. J.* 406:158

Burrows A, Marley MS, Sharp CM. 2000. *Ap. J.* 531:438

Burrows A, Sharp CM. 1999. *Ap. J.* 512:843

Caffau E, Ludwig HG, Steffen M, Freytag B, Bonifacio P. 2011. *Sol. Phys.* 268:255

Cannon CJ. 1973. *J. Quant. Spectrosc. Radiat. Transf.* 13:627

Carbon DF. 1979. *Annu. Rev. Astron. Astrophys.* 17:513

Castelli F, Gratton RG, Kurucz RL. 1997. *Astron. Astrophys.* 318:841

Catling DC. 2015. In *Treatise on Geophysics*, ed. G Schubert, Vol. 10, p. 429. Amsterdam: Elsevier. 2nd ed.

Cattaneo F, Brummell NH, Toomre J, Malagoli A, Hurlburt NE. 1991. *Ap. J.* 370:282

Chabrier G, Baraffe I. 1997. *Astron. Astrophys.* 327:1039

Chabrier G, Baraffe I, Allard F, Hauschildt P. 2000. *Ap. J.* 542:464

Chan KL, Sofia S, Wolff CL. 1982. *Ap. J.* 263:935

Chandrasekhar S. 1960. *Radiative Transfer*. Mineola, NY: Dover

Crossfield IJM, Biller B, Schlieder JE, et al. 2014. *Nature* 505:654

Currie T, Burrows A, Itoh Y, et al. 2011. *Ap. J.* 729:128

Cushing MC, Marley MS, Saumon D, et al. 2008. *Ap. J.* 678:1372

Domoto GA. 1974. *J. Quant. Spectrosc. Radiat. Transf.* 14:935

Evans KF, Stephens GL. 1991. *J. Quant. Spectrosc. Radiat. Transf.* 46:413

Fegley B Jr., Lodders K. 1994. *Icarus* 110:117

Fegley B Jr., Lodders K. 1996. *Ap. J. Lett.* 472:L37

Fortney JJ. 2012. *Ap. J. Lett.* 747:L27

Fortney JJ, Marley MS, Lodders K, Saumon D, Freedman R. 2005. *Ap. J. Lett.* 627:L69

Freedman RS, Lustig-Yaeger J, Fortney JJ, et al. 2014. *Ap. J. Suppl. Ser.* 214(2):25

Freedman RS, Marley MS, Lodders K. 2008. *Ap. J. Suppl. Ser.* 174:504

Freytag B, Allard F, Ludwig HG, Homeier D, Steffen M. 2010. *Astron. Astrophys.* 513:A19

Fu Q, Liou KN. 1992. *J. Atmos. Sci.* 49:2139

Fukabori M, Nakazawa T, Tanaka M. 1986. *J. Quant. Spectrosc. Radiat. Transf.* 36:265

Gabard T. 2013. *J. Mol. Spectrosc.* 291:61

Gamache RR, Hawkins RL, Rothman LS. 1990. *J. Mol. Spectrosc.* 142:205

Gamache RR, Lamouroux J. 2013. *J. Quant. Spectrosc. Radiat. Transf.* 130:158

Gamache RR, Lynch R, Brown LR. 1996. *J. Quant. Spectrosc. Radiat. Transf.* 56:471

Geballe TR, Saumon D, Golimowski DA, et al. 2009. *Ap. J.* 695:844

Gelino CR, Marley MS, Holtzman JA, Ackerman AS, Lodders K. 2002. *Ap. J.* 577:433

Gierasch P, Goody R. 1968. *Planet. Space Sci.* 16:615

Gierasch PJ, Conrath BJ. 1985. In *Recent Advances in Planetary Meteorology*, ed. GE Hunt, pp. 121–46. Cambridge, UK: Cambridge Univ. Press

Gillon M, Triaud AHMJ, Jehin E, et al. 2013. *Astron. Astrophys.* 555:L5

Goody R, West R, Chen L, Crisp D. 1989. *J. Quant. Spectrosc. Radiat. Transf.* 42:539

Goody R, Yung YL. 1989. *Atmospheric Radiation: Theoretical Basis*. New York: Oxford Univ. Press

Griffith CA, Yelle RV, Marley MS. 1998. *Science* 282:2063

Guillot T. 2010. *Astron. Astrophys.* 520:A27

Guillot T, Gautier D, Chabrier G, Mosser B. 1994. *Icarus* 112:337

Hanel RA, Conrath BJ, Herath LW, Kunde VG, Pirraglia JA. 1981. *J. Geophys. Res.* 86:8705

Hansen BMS. 2008. *Ap. J. Suppl. Ser.* 179:484

Hansen CJ, Kawaler SD, Trimble V. 2004. *Stellar Interiors: Physical Principles, Structure, and Evolution*. New York: Springer

Hansen JE. 1969. *Ap. J.* 155:565

Hauschildt PH. 1992. *J. Quant. Spectrosc. Radiat. Transf.* 47:433

Hauschildt PH, Lowenthal DK, Baron E. 2001. *Ap. J. Suppl. Ser.* 134:323

Heinze AN, Metchev S, Apai D, et al. 2013. *Ap. J.* 767:173

Helling C, Ackerman A, Allard F, et al. 2008a. *MNRAS* 391:1854

Helling C, Casewell S. 2014. *Astron. Astrophys. Rev.* 22:80

Helling C, Dehn M, Woitke P, Hauschildt PH. 2008b. *Ap. J. Lett.* 675:L105

Helling C, Oevermann M, Lüttke MJH, Klein R, Sedlmayr E. 2001. *Astron. Astrophys.* 376:194

Helling C, Woitke P. 2006. *Astron. Astrophys.* 455:325

Helling C, Woitke P, Thi WF. 2008c. *Astron. Astrophys.* 485:547

Heng K, Showman AP. 2015. *Annu. Rev. Earth Planet. Sci.* 43:509–40

Henyey L, Vardya MS, Bodenheimer P. 1965. *Ap. J.* 142:841

Huang X, Yung YL. 2004. *J. Atmos. Sci.* 61:1630–32

Hubbard WB, Burrows A, Lunine JI. 2002. *Annu. Rev. Astron. Astrophys.* 40:103

Hubbard WB, Smoluchowski R. 1973. *Space Sci. Rev.* 14:599

Hubeny I. 2003. In *Stellar Atmosphere Modeling*, ed. I Hubeny, D Mihalas, K Werner. *ASP Conf. Ser.* 288:17. San Francisco: ASP

Hubeny I, Burrows A. 2007. *Ap. J.* 669:1248

Hubeny I, Lanz T. 1992. *Astron. Astrophys.* 262:501

Hubeny I, Lanz T. 1995. *Ap. J.* 439:875

Husser TO, Wende-von Berg S, Dreizler S, et al. 2013. *Astron. Astrophys.* 553:A6

Kippenhahn R, Weigert A, Weiss A. 2012. *Stellar Structure and Evolution*. New York: Springer

Kirkpatrick JD. 2005. *Annu. Rev. Astron. Astrophys.* 43:195

Kondratyev KY. 1965. *Radiative Heat Exchange in the Atmosphere*. New York: Pergamon

Kurucz RL. 1996. In *Model Atmospheres and Spectrum Synthesis*, ed. SJ Adelman, F Kupka, WW Weiss, *ASP Conf. Ser.* 108:2. San Francisco: ASP

Lacis AA, Hansen J. 1974. *J. Atmos. Sci.* 31:118

Lacis AA, Oinas V. 1991. *J. Geophys. Res.* 96:9027

Le Moal MF, Severin F. 1986. *J. Quant. Spectrosc. Radiat. Transf.* 35:145

Leconte J, Chabrier G. 2012. *Astron. Astrophys.* 540:A20

Lee JM, Fletcher LN, Irwin PGJ. 2012. *MNRAS* 420:170

Lee JM, Heng K, Irwin PGJ. 2013. *Ap. J.* 778:97

Lenzuni P, Chernoff DF, Salpeter EE. 1991. *Ap. J. Suppl. Ser.* 76:759

Lewis JS. 1972. *Icarus* 16:241–52

Line MR, Fortney JJ, Marley MS, Sorahana S. 2014. *Ap. J.* 793:33

Line MR, Wolf AS, Zhang X, et al. 2013. *Ap. J.* 775:137

Line MR, Zhang X, Vasisht G, et al. 2012. *Ap. J.* 749:93

Liou KN. 1974. *J. Appl. Meteorol.* 31:522

Lodders K. 1999. *Ap. J.* 519:793

Lodders K. 2003. *Ap. J.* 591:1220

Lodders K. 2004. *Science* 303:323

Lodders K. 2010. In *Formation and Evolution of Exoplanets*, ed. R Barnes, p. 157. Hoboken, NJ: Wiley-VCH

Lodders K, Fegley B Jr. 2002. *Icarus* 155:393

Lodders K, Fegley B Jr. 2006. In *Astrophysics Update 2*, ed. JW Mason, p. 1. New York: Springer-Praxis

Ludwig HG, Allard F, Hauschildt PH. 2006. *Astron. Astrophys.* 459:599

Lunine JI, Hubbard WB, Burrows A, Wang YP, Garlow K. 1989. *Ap. J.* 338:314

Lunine JI, Hubbard WB, Marley MS. 1986. *Ap. J.* 310:238

Lupu R, Zahnle K, Marley MS, et al. 2014. *Ap. J.* 784:27

Macintosh BA, Anthony A, Atwood J, et al. 2012. In *Ground-based and Airborne Instrumentation for Astronomy IV*, ed. IS McLean, SK Ramsay, H Takami. *Proc. SPIE Conf. Ser.* 8446:84461U. Bellingham, WA: SPIE

Macintosh BA, Graham JR, Palmer DW, et al. 2008. In *Adaptive Optics Systems*, ed. N Hubin, CE Max, PL Wizinowich. *Proc. SPIE Conf. Ser.* 7015:701518. Bellingham, WA: SPIE

Madhusudhan N, Harrington J, Stevenson KB, et al. 2011. *Nature* 469:64

Madhusudhan N, Seager S. 2009. *Ap. J.* 707:24

Manabe S, Strickler RF. 1964. *J. Atmos. Sci.* 21:361

Manabe S, Wetherald RT. 1967. *J. Atmos. Sci.* 24:241

Margolis JS. 1993. *J. Quant. Spectrosc. Radiat. Transf.* 50:431

Margolis JS. 1996. *J. Quant. Spectrosc. Radiat. Transf.* 55:823

Marley MS. 2000. In *From Giant Planets to Cool Stars*, ed. CA Griffith, MS Marley, *ASP Conf. Ser.* 212:152. San Francisco: ASP

Marley MS, Ackerman AS, Cuzzi JN, Kitzmann D. 2013. In *Comparative Climatology of Terrestrial Planets*, ed. SJ Mackwell, AA Simon-Miller, JW Harder, MA Bullock, p. 391. Tucson: Univ. Ariz. Press

Marley MS, McKay CP. 1999. *Icarus* 138:268

Marley MS, Saumon D, Cushing M, et al. 2012. *Ap. J.* 754:135

Marley MS, Saumon D, Goldblatt C. 2010. *Ap. J. Lett.* 723:L117

Marley MS, Saumon D, Guillot T, et al. 1996. *Science* 272:1919

Marley MS, Seager S, Saumon D, et al. 2002. *Ap. J.* 568:335

McClatchey RA, Benedict WS, Clough SA, et al. 1973. *AFCRL atmospheric absorption line parameters compilation*. AFCRL-TR-0096, Environ. Res. Pap. 434, Air Force Cambridge Res. Lab., Bedford, MA

McKay CP, Pollack JB, Courtin R. 1989. *Icarus* 80:23

Meador W, Weaver W. 1980. *J. Atmos. Sci.* 37:630

Meadows VS, Crisp D. 1996. *J. Geophys. Res.* 101:4595

Mihalas D. 1970. *Stellar Atmospheres*. London: W. H. Freeman

Milkey RW, Shine RA, Mihalas D. 1975. *Ap. J.* 202:250

Mlawer EJ, Payne VH, Moncet JL, et al. 2012. *R. Soc. Lond. Philos. Trans. Ser. A* 370:2520

Mlawer EJ, Taubman SJ, Brown PD, Iacono MJ, Clough SA. 1997. *J. Geophys. Res.* 102:16663

Morley CV, Fortney JJ, Marley MS, et al. 2012. *Ap. J.* 756:172

Morley CV, Marley MS, Fortney JJ, Lupu R. 2014a. *Ap. J. Lett.* 789:L14

Morley CV, Marley MS, Fortney JJ, et al. 2014b. *Ap. J.* 787:78

Moses J. 2000. In *From Giant Planets to Cool Stars*, ed. CA Griffith, MS Marley. *ASP Conf. Ser.* 212:196. San Francisco: ASP

Niemann HB, Atreya SK, Carignan GR, et al. 1998. *J. Geophys. Res.* 103:22831

Noll KS, Geballe TR, Marley MS. 1997. *Ap. J. Lett.* 489:L87

Olson GL, Auer L, Buchler JR. 1986. *J. Quant. Spectrosc. Radiat. Transf.* 35:431

Oppenheimer BR, Kulkarni SR, Matthews K, van Kerkwijk MH. 1998. *Ap. J.* 502:932

Parmentier V, Guillot T. 2014. *Astron. Astrophys.* 562:A133

Pearl JC, Conrath BJ, Hanel RA, Pirraglia JA, Coustenis A. 1990. *Icarus* 84:12

Pecker JC. 1965. *Annu. Rev. Astron. Astrophys.* 3:135

Pierrehumbert RT. 2010. *Principles of Planetary Climate*. Cambridge, MA: Cambridge Univ. Press

Pollack JB, Dalton JB, Grinspoon D, et al. 1993. *Icarus* 103:1

Pollack JB, Rages K, Baines KH, et al. 1986. *Icarus* 65:442

Prandtl L. 1925. *Z. Angew. Math. Mech.* 5:136

Prinn RG, Barshay SS. 1977. *Science* 198:1031

Radigan J, Jayawardhana R, Lafrenière D, et al. 2012. *Ap. J.* 750:105

Rice EL, Barman T, Mclean IS, Prato L, Kirkpatrick JD. 2010. *Ap. J. Suppl. Ser.* 186:63

Richard C, Gordon IE, Rothman LS, et al. 2012. *J. Quant. Spectrosc. Radiat. Transf.* 113:1276

Robinson TD, Catling DC. 2012. *Ap. J.* 757:104

Robinson TD, Marley MS. 2014. *Ap. J.* 785:158

Rodgers CD. 1976. *Rev. Geophys. Space Phys.* 14:609

Rodgers CD. 2000. *Inverse Methods for Atmospheric Sounding: Theory and Practice*. Singapore: World Sci.

Rothman L, Gamache R, Goldman A, et al. 1987. *Appl. Opt.* 26:4058

Rothman L, Gordon I, Babikov Y, et al. 2013. *J. Quant. Spectrosc. Radiat. Transf.* 130:4

Rothman L, Gordon I, Barber R, et al. 2010. *J. Quant. Spectrosc. Radiat. Transf.* 111:2139

Rothman LS, Wattson R, Gamache R, Schroeder JW, McCann A. 1995. In *Atmospheric Propagation and Remote Sensing IV*, ed. JC Dainty. *Proc. SPIE Conf. Ser.* 2471:105. Bellingham , WA: SPIE

Satoh M. 2004. *Atmospheric Circulation Dynamics and General Circulation Models*. New York: Springer-Praxis

Saumon D, Bergeron P, Lunine JI, Hubbard WB, Burrows A. 1994. *Ap. J.* 424:333

Saumon D, Geballe TR, Leggett SK, et al. 2000. *Ap. J.* 541:374

Saumon D, Marley MS. 2008. *Ap. J.* 689:1327

Saumon D, Marley MS, Cushing MC, et al. 2006. *Ap. J.* 647:552

Schreier F. 2011. *J. Quant. Spectrosc. Radiat. Transf.* 112:1010

Schwarzschild K. 1906. *Math.-Phys. Klasse* 195:41

Sharp CM, Burrows A. 2007. *Ap. J. Suppl. Ser.* 168:140

Showman AP, Kaspi Y. 2013. *Ap. J.* 776:85

Smith MD. 1998. *Icarus* 132:176

Sorahana S, Suzuki TK, Yamamura I. 2014. *MNRAS* 440:3675

Sorahana S, Yamamura I. 2012. *Ap. J.* 760:151

Spiegel EA. 1971. *Annu. Rev. Astron. Astrophys.* 9:323

Stamnes K, Swanson RA. 1981. *J. Atmos. Sci.* 38:387

Stamnes K, Tsay SC, Wiscombe W, Jayaweera K. 1988. *Appl. Opt.* 27:2502

Stamnes K, Tsay SC, Wiscombe W, Laszlo I. 2000. *DISORT, a general-purpose Fortran program for discrete-ordinate-method radiative transfer in scattering and emitting layered media: documentation of methodology*. NASA Rep., NASA Goddard Space Flight Cent., New York

Stephens DC, Leggett SK, Cushing MC, et al. 2009. *Ap. J.* 702:154

Stevenson DJ, Salpeter EE. 1976. In *Jupiter: Studies of the Interior, Atmosphere, Magnetosphere and Satellites*, ed. T Gehrels, pp. 85–112. Tucson: Univ. Ariz. Press

Tennyson J, Yurchenko SN. 2012. *MNRAS* 425:21

Tinney CG, Tolley AJ. 1999. *MNRAS* 304:119

Toon OB, McKay CP, Ackerman TP, Santhanam K. 1989. *J. Geophys. Res.* 94:16287

Tsuji T. 1971. *Publ. Astron. Soc. Jpn.* 23:553

Tsuji T. 1984. *Astron. Astrophys.* 134:24

Tsuji T. 1994. In *Molecules in the Stellar Environment, IAU Colloq. 146, Lect. Notes Phys.* 428, ed. UG Jørgensen, pp. 79–97. New York: Springer

Tsuji T. 2002. *Ap. J.* 575:264

Tsuji T. 2005. *Ap. J.* 621:1033

Tsuji T, Ohnaka K, Aoki W, Nakajima T. 1996. *Astron. Astrophys.* 308:L29

Twomey S, Jacobowitz H, Howell HB. 1966. *J. Atmos. Sci.* 23:289

van de Hulst HC. 1963. *A new look at multiple scattering*. Tech. Rep., NASA Inst. Space Stud., Goddard Space Flight Cent., New York

van Zeggeren F, Storey SH. 1970. *The Computation of Chemical Equilibria*. Cambridge, UK: Cambridge Univ. Press

Vardya MS. 1970. *Annu. Rev. Astron. Astrophys.* 8:87

Visscher C, Lodders K, Fegley B Jr. 2006. *Ap. J.* 648:1181

Vitense E. 1953. *Z. Astrophys.* 32:135

West R, Crisp D, Chen L. 1990. *J. Quant. Spectrosc. Radiat. Transf.* 43:191

Winters BH, Silverman S, Benedict WS. 1964. *J. Quant. Spectrosc. Radiat. Transf.* 4:527

Wiscombe WJ. 1976. *J. Quant. Spectrosc. Radiat. Transf.* 16:477

Witte S, Helling C, Barman T, Heidrich N, Hauschildt PH. 2011. *Astron. Astrophys.* 529:A44

Wriedt T. 2012. In *The Mie Theory*, ed. W Hergert, T Wriedt, *Springer Ser. Opt. Sci.* 169:53–71. New York: Springer

Yamamoto G, Tanaka M, Asano S. 1970. *J. Atmos. Sci.* 27:282

Zahnle K, Marley M. 2014. *Ap. J.* 797:41

Zahnle K, Marley MS, Freedman RS, Lodders K, Fortney JJ. 2009. *Ap. J. Lett.* 701:L20

Zhang X, Showman AP. 2014. *Ap. J. Lett.* 788:L6

**Annual Review of
Astronomy and
Astrophysics**

Volume 53, 2015

Contents

Indexes

Errata

An online log of corrections to *Annual Review of Astronomy and Astrophysics* articles
may be found at http://www.annualreviews.org/errata/astro